iAtlantic
INTEGRATED ASSESSMENT OF ATLANTIC MARINE ECOSYSTEMS IN SPACE AND TIME

iAtlantic Deliverable 1.3

Quantitative assessment of near-seafloor flow dynamics and physical drivers for material and larval transport

Project acronym:	iAtlantic
Grant Agreement:	818123
Deliverable number:	D1.3
Deliverable title:	Quantitative assessment of near-seafloor flow dynamics and physical drivers for material and larval transport
Work Package:	1
Date of completion:	01.02.2024
Authors:	Christian Mohn, Franziska Schwarzkopf, Patricia Garcia Jimenez, Cova Orejas, Veerle Huvenne, Mia Schumacher, Irene Pérez-Rodríguez, Roberto Sarralde Vizuete, Luis J. López Abellán, Pedro Vélez Belchí, Andy Dale, Colin Devey, Lisa Skein, Jørgen L.S. Hansen, Eva Friis Møller, Arne Biastoch, Cyrien Lemaréchal, Guillaume Roullet, Jonathan Gula

This project has received funding from the European Union's Horizon 2020 research and innovation programme under grant agreement No 818123 (iAtlantic). This output reflects only the author's view and the European Union cannot be held responsible for any use that may be made of the information contained therein.

Contents

List of Acronyms

AABW	Antarctic Bottom Water
AAIW	Antarctic Intermediate Water
ABNJ	Areas Beyond National Jurisdiction
ACC	Antarctic Circumpolar Current
CDW	Circumpolar Deep Water
COADS	Comprehensive Ocean-Atmosphere Data Set
CTD	Conductivity, Temperature, and Depth
EOS	Equations of State
ESACW	Eastern South Atlantic Central Water
LES	Large Eddy Simulations
LS	Lucky Strike
MTT	Morton Taylor Turner
NADW	North Atlantic Deep Water
NBL	Neutral Buoyancy Level
NE	Noth-East
NEMO	Nucleus For European Modelling of The Ocean
OTIS	Osu (Oregon State University) Tidal Inversion Software
ROMS-AGRIF	Regional Ocean Modelling System with Adaptive Grid Refinement In Fortran
RV	Research Vessel
SEAFO	South-East Atlantic Fisheries Organisation
SW	South-West
TKE	Turbulent Kinetic Energy
VME	Vulnerable Marine Ecosystem
WP	Work Package
WSBW	Weddell Sea Bottom Water

List of Tables

List of Figures

Executive Summary

As part of the EU Horizon 2020 iAtlantic project (Work Package (WP) 1, Deliverable 1.3 – '*Quantitative assessment of near-seafloor flow dynamics and physical drivers for material and larval transport*'), high to ultra-high hydrodynamic models were developed in two topographically and environmentally complex study regions to provide the fine-scale hydrodynamic context of biophysical and geophysical interactions with seafloor topography, which is often missing in basin-scale and regional-scale models. The models were conceived at the Lucky Strike vent field in the North Atlantic (iAtlantic Study Region 3) and at the Walvis Ridge in the South Atlantic (iAtlantic Study Region 9) to address the challenges of resolving processes at different spatial and temporal scales.

At the Walvis Ridge, two nested high-resolution implementations of the hydrodynamic model ROMS-AGRIF (Regional Ocean Modelling System with grid refinement) were employed aiming to identify and quantify the physical drivers of the distribution of benthic cold-water coral communities at spatial scales of several metres vertically to several hundreds of metres horizontally. In contrast to Walvis Ridge, the task of modelling the plume dynamics at the Lucky Strike vent field focussed on the vertical motion from injection of hydrothermal tracers at the vent to the neutral level, where the hydrothermal material is then dispersed horizontally. The vertical motion is due to the turbulent buoyant plume. To study this plume, large eddy simulations (LES) with grid sizes down to 1 cm were analysed to resolve the outlet of a deep-sea vent. LES were performed using the Basilisk code, an open-source model code for solving partial differential equations of motion on adaptive Cartesian meshes.

The original plan of WP1-Deliverable 1.3 was designed for the use of the non-hydrostatic regional ocean model CROCO-NH as a model for both regions. For technical reasons, in particular related to the strong numerical noise in the vertical velocity field in areas of complex bathymetry preventing longer-term simulations, the integrations for the Walvis Ridge (Chapter 1) were using hydrostatic version of CROCO-NH, ROMS-AGRIF. In contrast, the work for the Lucky Strike vent field required the use of a non-hydrostatic code at the scale of a few metres. The use of an LES technique enabled an important pilot study for a better understanding of such ecosystems in the future. Both modelling studies addressed the role of hydrodynamic processes and mechanisms at very fine scales for the distribution of benthic communities and vent plume propagation at great detail, and thus provide a significant step forward to better evaluate the importance of flow-topography interactions in very complex marine systems.

The main conclusion of part 1 of this study is that increasing resolution horizontally and vertically close to the seafloor is an important advancement for precisely evaluating the intrinsic dynamics within challenging, rough terrain such as the Walvis Ridge seamounts. We found that the dissipation of kinetic energy in near-bottom ocean currents and internal wave dynamics may serve as effective proxies of food supply to cold-water corals and sponge communities. Our findings suggest that the predictive capacity of species distribution models for benthic communities may be improved by considering physical processes in addition to more traditional descriptors like water mass and terrain properties, thus enhancing our ability to predict the occurrence of benthic species communities in general.

The main conclusion of part 2 is that the simplified classical 1D model, so called MTT model, fails at predicting important features of the plumes at Lucky Strike, such as its height. The LES confirm that an entrainment rate of 0.13 in the lazy part of the plume is appropriate for the 1D model, but that a value of 0.04 would be more appropriate in the first metre near the vent. The LES shows that the vertical speed increases in the first metres but that to correctly represent this acceleration, it is crucial to include a full nonlinear equation of state. The LES also reveals that the Lucky Strike plumes have a very large mixing efficiency, typically 0.7, in the first 10 metres of its ascent, well above the oceanic standard value of 0.16, which emphasises the extraordinary regime of hydrothermal plumes compared to the rest of the ocean processes.

Chapter 1. Study Region 9: Bottom currents and bio-physical connections at two Walvis Ridge seamounts, Valdivia Bank and Ewing Seamount

Christian Mohn[1], Franziska Schwarzkopf [2], Patricia Garcia Jimenez[3], Cova Orejas[4], Veerle Huvenne[5], Mia Schumacher[2], Irene Pérez-Rodríguez[6], Roberto Sarralde Vizuete[6], Luis J. López Abellán[7], Pedro Vélez Belchí[7], Andy Dale[8], Colin Devey[2], Lisa Skein[9], Jørgen L.S. Hansen[1], Eva Friis Møller[1], Arne Biastoch[2]

[1]Department of Ecoscience, Aarhus University, Roskilde, Denmark
[2]GEOMAR Helmholtz Centre for Ocean Research Kiel, Kiel, Germany
[3]Tragsatec, Baleares Island, Spain.
[4] Centro Oceanográfico de Gijon, Instituto Español de Oceanografía, IEO-CSIC, Spain
[5]Ocean BioGeosciences, National Oceanography Centre, Southampton, UK (NOC)
[6] Centro Oceanográfico de Vigo, Instituto Español de Oceanografía, IEO-CSIC, Spain
[7] Centro Oceanográfico de Canarias, Instituto Español de Oceanografía, IEO-CSIC, Spain
[8] Scottish Association for Marine Science, Oban, United Kingdom
[9]Marine Programme, South African National Biodiversity Institute, Kirstenbosch Research Centre, Kirstenbosch National Botanical Gardens, Cape Town, South Africa

1.1. Abstract

This chapter presents a summary of the work carried out under Work Package 1, Deliverable 1.3 '*Quantitative assessment of near-seafloor flow dynamics and physical drivers for material and larval transport*'. At the Walvis Ridge (iAtlantic Study Region 9), we developed two nested high-resolution hydrodynamic models to study potential physical drivers of distribution of benthic filter feeding communities in two sub-regions of the Walvis Ridge: Valdivia Bank and Ewing Seamount. Spatial resolution in each model region was increased across two levels of nested grids with 1,500 m (parent grid) and 500 m (child grid) resolution. In the vertical, each model grid is composed of 32 stretched terrain-following (s-) layers with high resolution close to the bottom. The parent grid received initial conditions and lateral boundary conditions from the basin-scale model INALT20 and data from tidal model solutions using the OTIS inverse tidal model. The model topography consisted of the global GEBCO_2020 terrain model with local refinements using multi-beam data collected at different surveys at Valdivia Bank and Ewing Seamount from 2008 to 2010. Model simulations were completed for a simulation period covering the years 2007–2010 (with 2007 as spin-up). CTD data from Valdivia Bank surveys (IEO-CSIC, 2008–2010) were used to validate results from the local area model simulations against observed water mass properties. Results from both the local high-resolution ROMS-AGRIF and the INALT20 simulations showed very good agreement with observed T/S properties. The model simulations were used to quantify the dominant scales of temporal and spatial variability of the near-bottom currents at Valdivia Bank and Ewing Seamount and to test the capacity of functional proxies for predicting presence and absence of observed benthic communities in both areas. We found that physical proxies representing drivers and mechanisms of food supply (e.g., kinetic energy dissipation, internal wave slope criticality) are important descriptors to predict the distribution of sessile benthic species occurrences. These functional proxies are proposed as additional descriptors to water mass properties such as temperature, salinity, and current speed, which are traditionally used in species distribution modelling.

1.2. Introduction

The global ocean seafloor is covered with countless isolated topographic elevations, from smaller knolls only several hundred metres high to intermediate and large seamounts rising several thousand metres above the seafloor occasionally entering the photic zone (Gevorgian et al., 2023; Wessel et al., 2010). Even though we know that large numbers exist, we still know surprisingly little about the structure and functioning of seamount ecosystems (Rogers, 2018). Some Atlantic seamounts have been well investigated (e.g., Christiansen and Wolff, 2009; Simpson and Watling, 2011; Giacomello et al., 2013) but Southeast Atlantic seamounts have been less well studied and only very few data on benthic communities, fish and environmental water column data exist, or data documentation is missing (Bergstad et al., 2019a, 2019b). However, significant progress has recently been made in these areas.

As part of various sampling programs in limited subregions of the South Atlantic, spatially resolved data on geology, benthos, fish, seabirds, and water mass properties were collected at the summits of the Valdivia Bank and at Ewing Seamount from 2008 to 2010 through the Spanish-Namibian collaborative effort RAP-SUR (López Abellán and Holtzhausen, 2011). Bergstad et al. (2019a) described the benthic megafauna and benthopelagic fish fauna at Valdivia Bank and Ewing Seamount as part of an extended survey of different Southeast Atlantic seamounts. Recent advances in other regions provided first insights of meso- and benthopelagic fish dynamics at remote seamounts in the South Atlantic from a combination of fisheries acoustic methods and pelagic trawl sampling (Campanella et al., 2021). Other EAF-Nansen surveys have been carried out in the Southeast Atlantic in 2019 and 2022 aiming at mapping and identification of Vulnerable Marine Ecosystems (VMEs) and fisheries resources in the Southwest Discovery Seamounts and the North Guinea Seamount chain respectively (SEAFO, 2019, 2022).

Despite these recent advances, the South Atlantic is still considered an area poor in data on physical oceanography, benthic species, and benthic ecosystem functioning. Modern dynamic and mechanistic basin-scale ocean models, spatially explicit broad-scale benthic habitat classification techniques and multivariate benthic landscape maps have been increasingly used to narrow existing data gaps in the South Atlantic from coastal areas to Areas Beyond National Jurisdiction (ABNJ) (Tim et al., 2018; Rühs et al., 2019; Schumacher et al., 2022; McQuaid et al., 2023). In this study, we combined data from a high-resolution nested implementation of the hydrodynamic ROMS-AGRIF model (Shchepetkin and McWilliams, 2005) with macrobenthos species occurrences in the near-bottom layers at Valdivia Bank and Ewing Seamount. We described the dominant oceanographic patterns and their spatial and temporal variability and investigated bio-physical connections and physical drivers of benthic megafauna distributions in each area. The local hydrodynamic models have a resolution of 1,500 m (parent grid) and 500 m (child grid), and received input from high-resolution bathymetry, barotropic tides and water mass properties. The region is connected to the open ocean, in particular the South Atlantic subtropical gyre and the influence from the Indian Ocean through the Agulhas Current system, called Agulhas leakage (Rühs et al., 2022). The information of the embedding is provided through lateral boundary conditions of velocities and hydrography from the basin-scale ocean general circulation model INALT20 with a resolution of 1/20° (Schwarzkopf et al., 2019, Rühs et al., 2022).

1.3. Materials & Methods

Study sites

Locations, bathymetry and benthos

Valdivia Bank is an elongated oceanic plateau located at the NE Walvis Ridge, a ridge system intersected by canyons and seamounts in the Southeast Atlantic and separating the Angola Basin to the North from the Cape Basin to the South (Figure 1). The Valdivia Bank plateau has an elliptical shape with water depths ranging from 220 m to > 4,000 m in the surrounding abyssal plain (Bergstad et al., 2019b; Contreras et al., 2022). The entire plateau extends over a length of 360 km in the N-S direction (major axis) and 220 km in the E-W direction (minor axis). The bank morphology is characterised by generally gentle slopes of <1°, but there are several areas where slopes are significantly steeper exceeding 30° (Contreras et al., 2022). Along these steep slopes abrupt increases in depth of 1,500 m or greater are common (Contreras et al., 2022). The central summit plateau is composed of sub-regions with several isolated topographic elevations of different sizes and height. A prominent seamount-like feature is located at the southern plateau at approximately 6.4°E and 26.2°S (Figure 1a). This seamount is elongated in the NE-SW direction and has the form of a flat-topped guyot bounded by steep slopes with water depths in the range 220 m to 1,000 m. Ewing Seamount is an isolated seamount located off the NE section of the Walvis Ridge in the northern Cape Basin cantered at 23.245 °S and 8.27 °E (Figure 1 b). It has a diameter of approximately 30 km and has an irregular and complex shape with inlets and rifts along the deeper slopes. The summit plateau covers a depth range of 850 to 1,000 m with a small summit peak at 780 m.

In limited subregions of the Valdivia Bank and Ewing Seamount (open to fisheries) spatially resolved data on physical oceanography, geomorphology, macrobenthos and benthopelagic fishes were collected during several Spanish-Namibian surveys in the years 2008, 2009 and 2010 to locate and describe VMEs associated with seamounts in the SEAFO Regulatory Area (López Abellán and Holtzhausen, 2011; Durán Muñoz et al., 2012; Figures 1 and 7). The two seamounts were visited again in 2015 as part of an extended survey of South Atlantic seamounts on board RV *Fridtjof Nansen* (Bergstad et al., 2019a). Analysis of samples from benthos surveys at Valdivia Bank (box-corer, rock-dredge, video and still photographs) showed that the three most common taxa were Hydrozoa, Actiniaria and Asteroidea, followed by Cirripedia and Bivalvia, but also with some occurrences of organisms belonging to the families Isididae (bamboo corals) and Echinoidea (Figure 1a; López Abellán and Holtzhausen, 2011). The most common species identified in benthos samples from Ewing Seamount belonged to the groups Echinothuridae and Zoantharia associated with the hermit crab *Parapagurus pilosimanus*. Specimens of Hydrozoa, Gorgonacea and Echinoidea were also described (López Abellán and Holtzhausen, 2011). Bergstad et al. (2019a) described large diversity in benthic megafauna associated with Southeast Atlantic seamounts with ancient scleractinian coral framework and rubble. Camera surveys at Valdivia Bank showed that live corals were very patchily distributed, and numbers often decreased towards the summits, except for the shallow southeast Valdivia summit in Figure 1, where numerous soft gorgonians were detected (Bergstad et al., 2019a). At Ewing Seamount, scattered live corals (scleractinians, gorgonians and antipatharians) were recorded during all camera surveys, again with decreasing numbers at the seamount summit (Bergstad et al., 2019a).

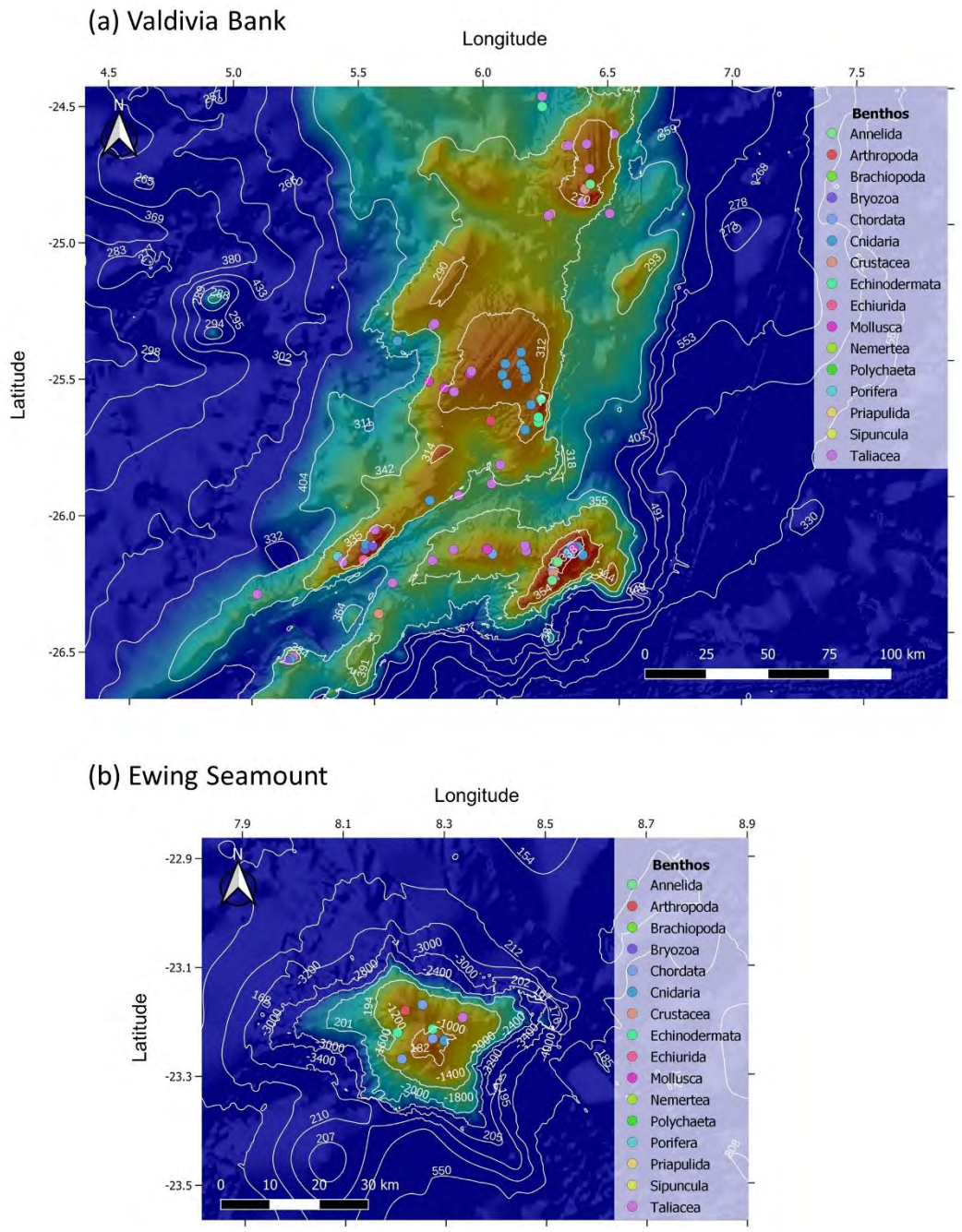

Figure 1. Bathymetric maps of the central Valdivia Bank plateau (a) and Ewing Seamount (b) showing benthos sampling locations and benthos distribution highlighted by coloured circles. Benthic sampling was conducted in the period 2008–2010 by IEO-CSIC (Spain) as part of the RAP-SUR project (López Abellán and Holtzhausen, 2011).

Water masses and major circulation patterns

CTD data from the Valdivia Bank collected during the 2008–2010 RAP-SUR project are displayed in a potential temperature – salinity (θ-S) diagram in Figure 2 (maps of all CTD station locations in both areas are presented in Figure 7). The water mass characteristics in the Valdivia Bank region largely correspond to properties found in other areas of the South Atlantic. Eastern South Atlantic Central Water (ESACW) is the main water mass in the upper layer and is cantered in the depth range 200 m–700 m. In the Valdivia Bank area, it covers the temperature and salinity range θ = 6–15 °C and S = 34.5–35.4, respectively, at densities σ_θ between 26.2 and 27.1 kg m^3 (Figure 2). ESACW is formed southwest of

South Africa, where the Agulhas Current carrying waters from the Indian Ocean mixes with the South Atlantic Current inside an area from 30-40° S and 0-20° E (Liu and Tanhua, 2021; and references therein). The minimum θ and S inflection point at θ = 4 °C, S = 34.4 and σ_θ = 27.3 kg m^3 represents the influence of Antarctic Intermediate Water (AAIW). AAIW is formed in the surface region north of the Antarctic Circumpolar Current (ACC), from where it subducts and propagates northward, while it is modified through mixing with surrounding water masses (Stramma and England, 1999; Liu and Tanhua, 2021). Below 1,200 m depth, the increase in salinity until the deep salinity maximum S = 34.85 can be attributed to North Atlantic Deep Water (NADW), which covers the depth range 1,200 to 2,000 m in the South Atlantic and is composed of characteristic water masses from the North Atlantic overflow regions (Liu and Tanhua, 2021; and references therein). The deepest waters in the Valdivia Bank region showed inflections of Antarctic Bottom Water (AABW) at a temperature minimum of θ = 2.8 °C. AABW is formed in the Weddell Sea region through mixing of Circumpolar Deep Water (CDW) and Weddell Sea Bottom Water (WSBW) (van Heuven et al., 2011). As part of the Walvis Ridge, Valdivia Bank and Ewing Seamount are affected by the anticyclonic circulation in the South Atlantic subtropical gyre (Chidichimo et al. 2023). Additionally, a potentially important impact comes from the southeast, where warm and salty waters of Indian Ocean origin enter the Atlantic Ocean through Agulhas Leakage (Rühs et al., 2022). This happens as direct inflow but also in the form of large mesoscale eddies. These 'Agulhas rings' represent one of the largest mesoscale eddies in the world ocean, with diameters of more than hundred kilometres and depth extensions of 1,000 m and more (Casanova-Masjoan et al., 2017). The Walvis Ridge lies in the northeast of the main path along which Agulhas rings drift into the South Atlantic (Dencausse et al. 2010). Even though during the course of the experiment, very few anticyclonic eddies barely touch the southwestern region of the regional model, the warm and saline conditions of the Agulhas Current system are quite present as is shown above.

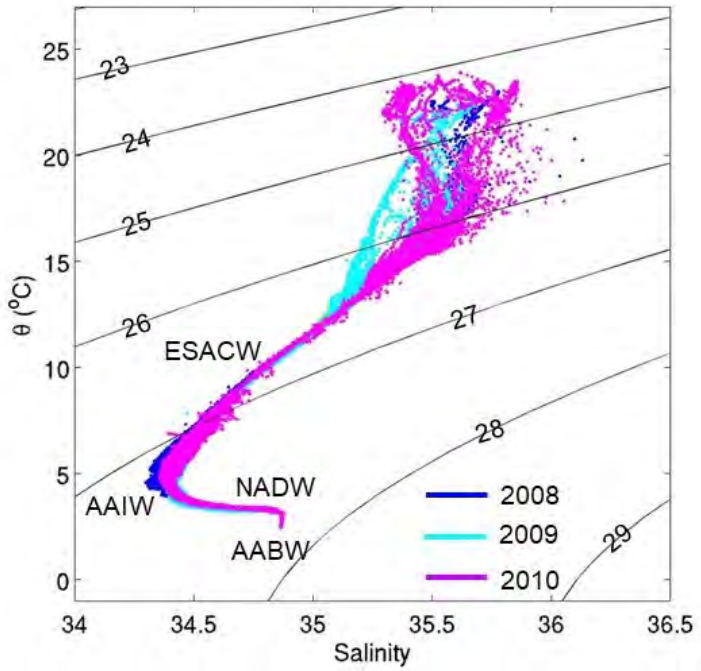

Figure 2. Salinity vs. potential temperature θ (°C) of CTD data from the 2008–2010 RAP-SUR. Coloured dots indicate data from different years, black lines denote isopycnals of density anomaly σ_θ (kg m^{-3}). The water masses shown are Eastern South Atlantic Central Water (ESACW), Antarctic Intermediate Water (AAIW), North Atlantic Deep Water (NADW) and Antarctic Bottom Water (AABW).

Barotropic tides

Barotropic tidal currents and tidal ellipse parameters were calculated from time series for the period January–March 2009 extracted from the North Atlantic solution AO_atlas (1/12° spatial resolution) of the Oregon State University Tidal Inversion Software (OTIS; Egbert and Erofeeva, 2002). We displayed the dominant semidiurnal (M2, period = 12.4 h) and diurnal (K1, period = 23.9 h) tidal constituents to highlight the tidal characteristics in the wider study area (Figure 3). The major axes of the tidal ellipses are directed NNW to SSE in the deep basins, but less aligned with the topography over Valdivia Bank. The magnitude of the M2 major axis is typically larger by one order of magnitude than the K1 major axis. The maximum semi-major axis of the dominant semidiurnal tidal harmonic M2 is up to 2 cm/s above the shallow parts of the Valdivia Bank between 5° and 7° E and -23° and -27° S, whereas the minimum semi-major M2 axes is 1.1 cm/s in the Cape Basin (Figure 3a). The main diurnal tidal harmonic K1 is an order of magnitude smaller (maximum semi-major axis 0.2 cm/s) and is strongly rectified in a North-South direction (Figure 3b).

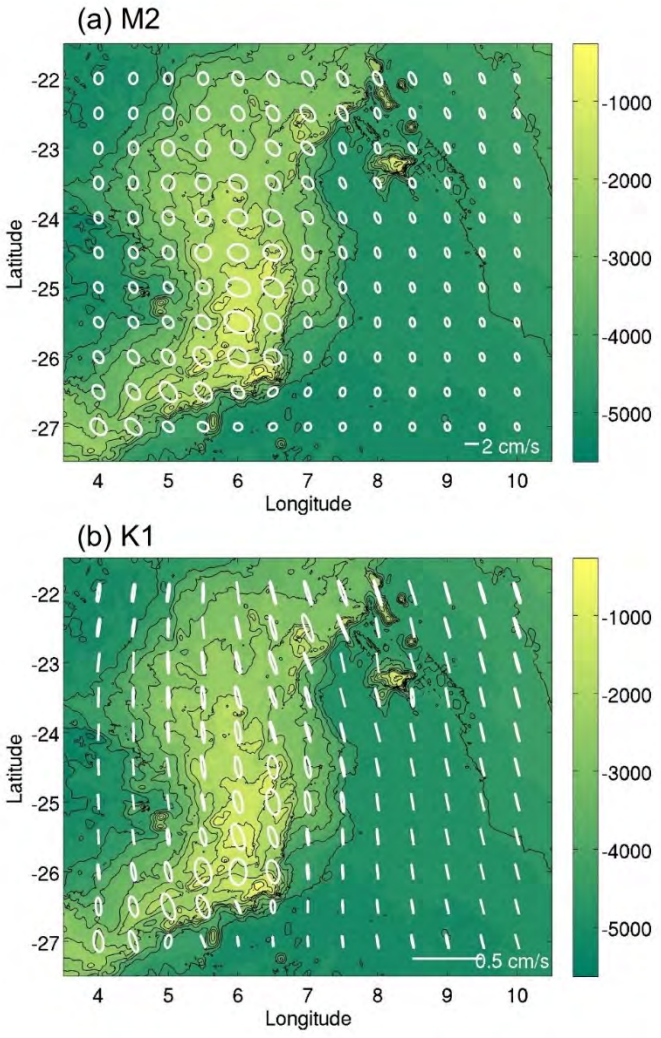

Figure 3. Current ellipses for the barotropic M2 (a) and K1 (b) tides from the Atlantic solution AO_atlas of the Oregon State University Tidal Inversion Software (OTIS). Coloured contours represent the bathymetry and black lines show depth contours from 500 to 6,000 m in 500 m intervals.

Hydrodynamic Model

The Regional Ocean Modelling System with grid refinement (ROMS-AGRIF, here version 3.1) was used to simulate currents and water mass properties at Valdivia Bank and Ewing Seamount with high resolution increasing across two levels of nested grids of 1,500 m and 500 m resolution in each study area (Figures 4, 5). ROMS-AGRIF is a free surface, finite difference, primitive equation model applying orthogonal curvilinear coordinates on a staggered Arakawa C-grid in the horizontal and stretched sigma coordinates (s-coordinates) in the vertical (Shchepetkin and McWilliams, 2005). The ROMS-AGRIF model receives initial conditions and lateral boundary conditions from the basin-scale model INALT20 (Schwarzkopf et al., 2019). Lateral boundary conditions are provided as five-day averages of current velocities, regional sea surface height, temperature, and salinity (Figure 4).

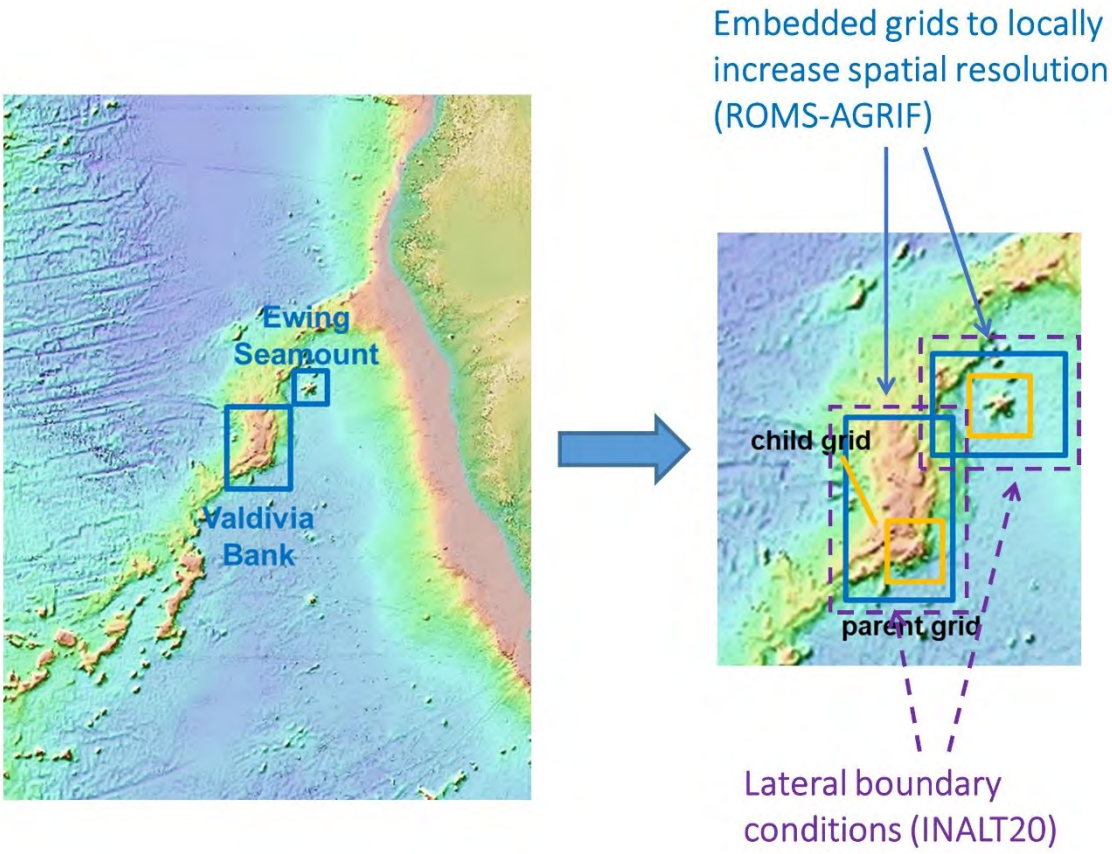

Figure 4. Location of the model areas Valdivia Bank and Ewing Seamount in iAtlantic Study Region 9 along the Walvis Ridge in the Southeast Atlantic (left). The ROMS-AGRIF model employs embedded grids in two sub-regions to locally increase spatial resolution with improved bathymetry (right). The ROMS-AGRIF parent grids (1,500 m spatial resolution) receive lateral boundary conditions from the basin-scale INALT20 model. The ROMS-AGRIF local nests (child grids) receive lateral boundary conditions from the parent grid.

INALT20 is a global eddy-permitting (1/4°) ocean/sea ice model configuration based on NEMO (Nucleus for European Modelling of the Ocean) with a high-resolution eddy-rich nest (1/20°) covering the South Atlantic and the western Indian oceans between 70°W and 70°E and extending from the northern tip of the Antarctic Peninsula at 63°S to 10°N (Schwarzkopf et al., 2019). For our local simulations, we used a hindcast simulation in INALT20 (referred to as SIM_{JRA0} in Rühs et al., 2022) driven by the recent atmospheric forcing product JRA55-do (Tsujino et al. 2018). The OSU inverse tidal model provides instantaneous sea surface height and barotropic velocities for 10 tidal constituents (Egbert and

Erofeeva, 2002) through radiation terms along the open lateral boundaries. Local solutions of water mass properties and currents from the parent grids at 1,500 m resolution were transferred to the child grids at 500 m resolution at every time step using the same open boundary radiation terms. Explicit lateral viscosity is zero everywhere in the models except one grid cell wide sponge layer on each grid to reduce numerical instabilities along the open boundaries. COADS (Comprehensive Ocean-Atmosphere Data Set, 0.5° x 0.5° spatial resolution) data were used as background atmospheric forcing at the free surface. The total simulation time was set to four years covering the period 2007 to 2010. Between 2008 and 2010, extensive field work including data from physical oceanography, multibeam and benthos were collected at Valdivia Bank and Ewing Seamount (López Abellán and Holtzhausen, 2011). The largest model time step is 90 seconds, which is sufficient to capture tidal dynamics as an important physical driver at these sites. The bathymetry used in the model is an integrated dataset from multibeam surveys collected between 2008 and 2010 by IEO-CSIC as part of the RAP-SUR project in both study areas merged with depths predicted from the GEBCO_2020 global bathymetry at 15 arc seconds spatial resolution. GEBCO_2020 was the most recent version of the global bathymetry at the time of model setup. GEBCO's current global bathymetric data set is the GEBCO_2022 Grid. The integrated bathymetry has a spatial resolution of 250 m. This bathymetry in combination with improved spatial resolution in the local nests allows a more detailed view of physical processes over complex topography in the central seamount areas of Valdivia Bank and Ewing Seamount (Figure 5). Table 1 summarises the grid metrics including size and number of horizontal grid points for each nested model domain.

Table 1. Grid metrics (size of model area and number of grid cells) of local high-resolution ROMS-AGRIF model implementations presented in Figure 5.

Grid geometry	Valdivia Bank (parent grid)	Valdivia Bank (child grid)	Ewing Seamount (parent grid)	Ewing Seamount (child grid)
Horizontal resolution (m)	1,500	500	1,500	500
Grid size [lon, lat] (km)	297 x 363	115 x 91	357 x 387	133 x 133
Grid points [lon, lat]	198 x 242	230 x 182	238 x 258	266 x 266
Longitude range (° E)	4.6 to 7.5	5.6 to 6.8	6.5 to 10.0	7.5 to 8.85
Latitude range (° N)	-27.19 to -23.76	-26.61 to -25.813	-24.96 to -21.488	-23.871 to -22.677

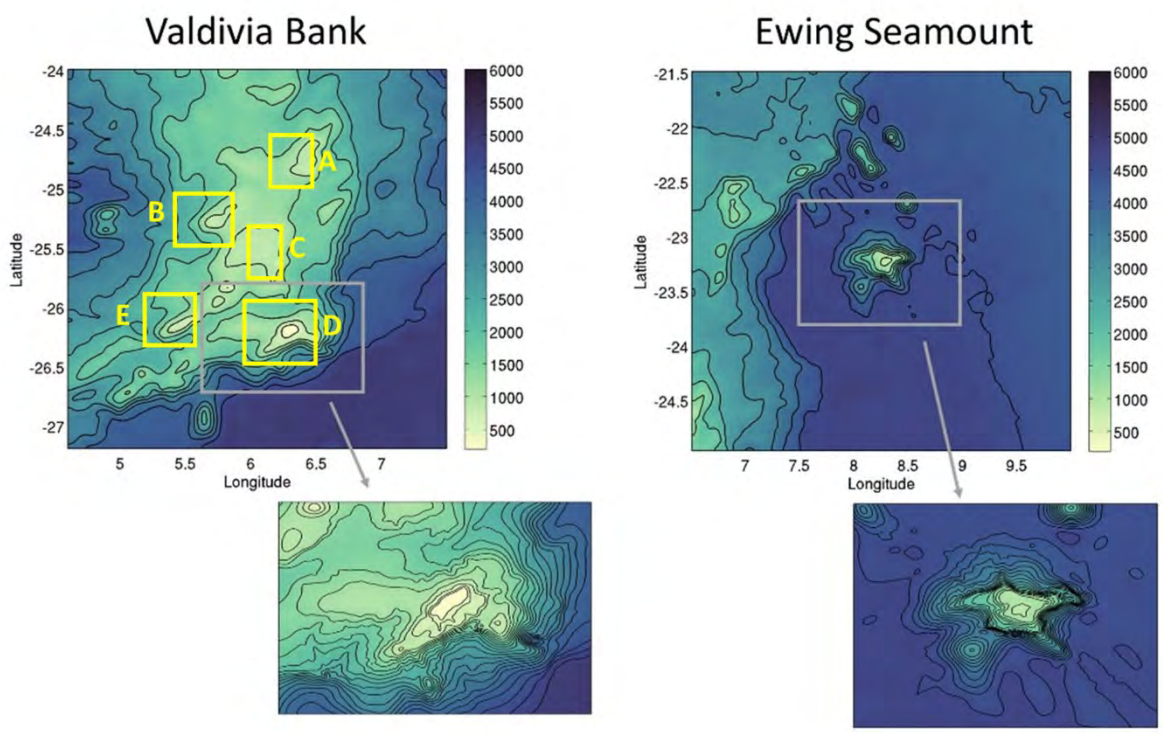

Figure 5. Local high resolution model implementations in iAtlantic Study Region 9 (Walvis Ridge). Left: Valdivia Bank, right: Ewing Seamount. Top: Parent grid – 1,500 m spatial resolution; bottom: Child grid – 500 m spatial resolution). The bathymetry of the child grid is an integrated dataset consisting of GEBCO_2020 and local multibeam data collected by IEO-CSIC Spain. Yellow rectangles represent the 2008–2010 sampling areas as part of the RAP-SUR project (López Abellán and Holtzhausen, 2011).

All nested model implementations have 32 terrain-following vertical layers (s-layers) with higher resolution close to the surface (stretching parameter θ_s = 3.4) and bottom (θ_b = 1.0). The s-layers vary with water depth from < 2 m and approximately 6.5 m in the shallowest areas of Valdivia Bank and Ewing Seamount, approximately 20–22 m over steep slopes, to 37–40 m over the deepest areas in each model domain respectively (Table 2 and Figure 6).

Table 2. Resolution (m) of the vertical s-layers in different model grids over different parts of the model bathymetry (h_{min} = minimum depth in each model grid, h_{max} = maximum depth in each model grid).

Grid	Δz (bottom) at h_{min}	Δz (bottom) over slopes	Δz (bottom) at h_{max}
Valdivia Parent	1.3	20.4	39.5
Valdivia Child	1.8	20.4	39.0
Ewing Parent	6.5	22.4	38.2
Ewing Child	6.7	22.1	37.5

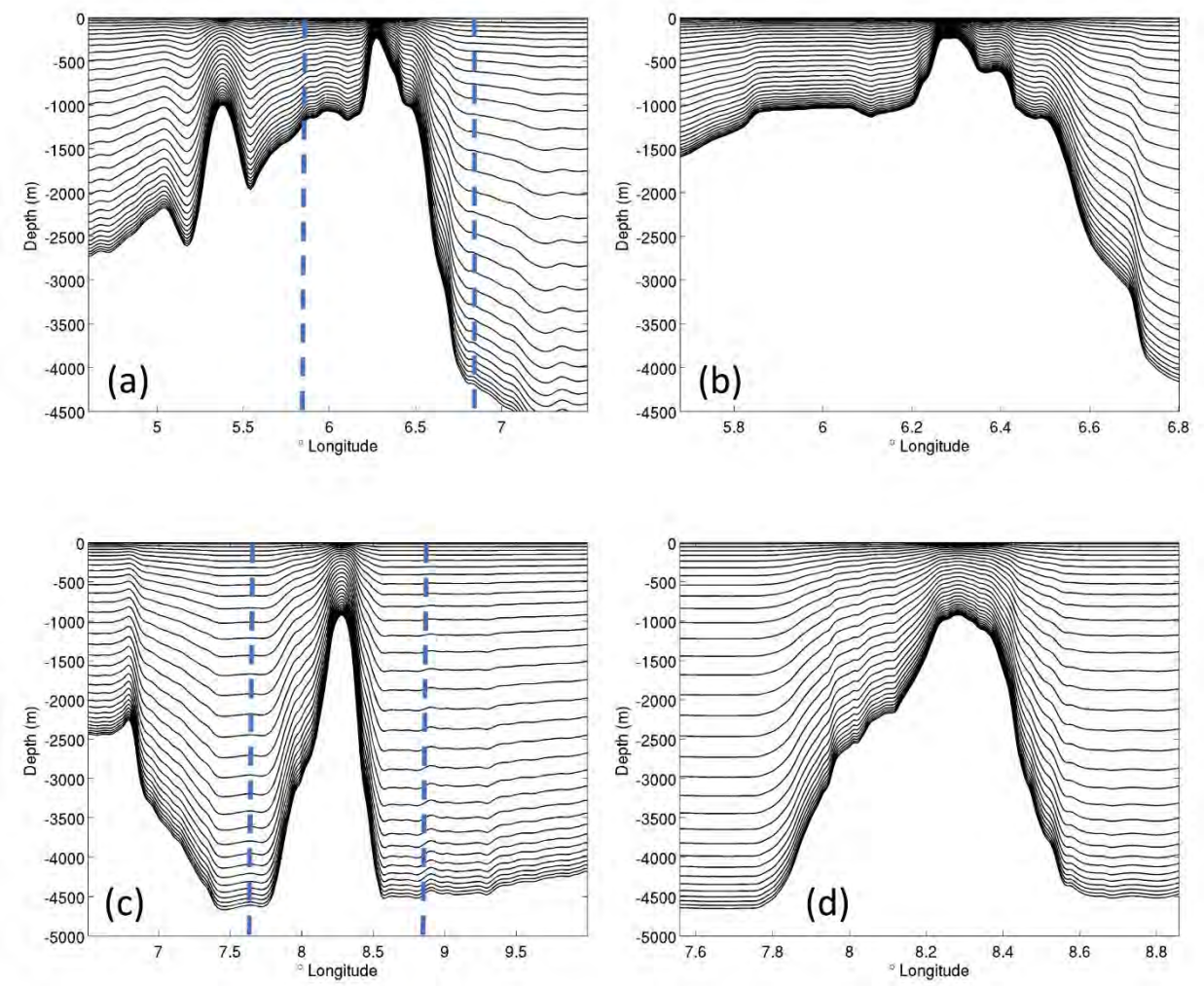

Figure 6. Vertical s-coordinate system (Depth vs Longitude) of the Valdivia parent (a) and child model (b), Ewing Seamount parent (c) and child model (d). All model grids employ 32 vertical levels with varying layer thickness. The transects were extracted at the central seamount regions at Valdivia Bank (sampling area D) and Ewing Seamount. The blue dashed lines in (a) and (c) indicate the lateral boundaries of the child grid in (b) and (c).

Field Measurements

Samples obtained from the three multidisciplinary Spanish-Namibian research cruises (2008–2010; López Abellán and Holtzhausen, 2011) were collected using trawl nets (bottom trawl and beam trawl), rock dredges and CTDs. Hydrographic data sampling was conducted along perpendicular transects over each seamount, with a regular 2' x 2' grid in the shallower areas, decreasing the distance between stations as depth increased. A Sea-Bird 25 CTD was used, which allowed measurements of physico-chemical properties of the water column including temperature, salinity, fluorescence, oxygen, density, and pressure at a total of 136 stations over the three surveys. The depth range of the stations was between 900 and 2,900 m (Figure 7).

Benthos samples were collected with bottom trawls (Lofoten-type otter trawls of 30 minutes duration at an average speed of 3 knots), beam trawls ('Bou de varas') of 30 minutes duration at an average speed of 1.7 knots and rock dredge trawls of 15 minutes duration at a speed of 1.7 knots. A total of 46 (4), 16 (1) and 15 (4) sets were made by gear respectively (in brackets the number of invalid sets). Haul location in decimal degrees is the estimated middle position of the whole path of sampling device for

trawling gears (Lofoten and beam trawl), but the final track point for the dredge sets, assuming that this is the exact point where a rock and probably an outcrop has been found making mandatory the hauling of the gear to not losing it. These seafloor positions have been mapped considering the vessel path and the actual position of the sampling device and considering trawling cable length *c* and depth *d*, to estimate the net position at the bottom according to $d=(c^2-a^2)^{1/2}$.

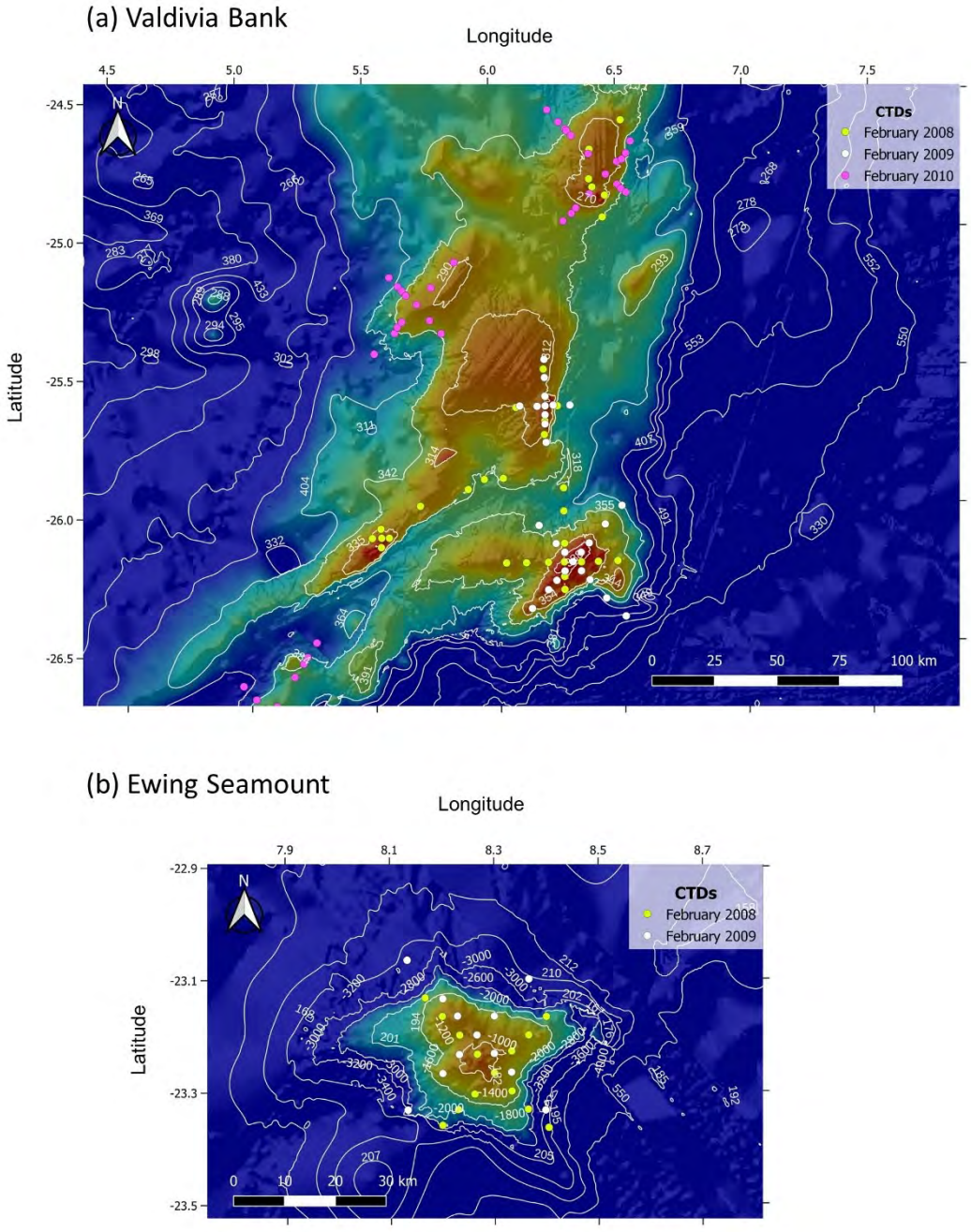

Figure 7. Positions of CTD stations sampled in the period 2008–2010 by IEO-CSIC (Spain) as part of the RAP-SUR project (López Abellán and Holtzhausen, 2011). (a) Valdivia Bank, (b) Ewing Seamount.

1.4. Results

Model-Data Comparison

Water mass properties based on CTD data from measurements in different sub-regions of Valdivia Bank were compared with corresponding model data (see Figure 7 for an overview of CTD station locations and sampling periods). We used daily averaged output from both the local area ROMS-AGRIF model (parent grid, 1,500 m spatial resolution) and the basin-scale INALT20 model (1/20 ° spatial resolution corresponding to a length scale of approximately 4 km) for this comparison. We extracted temperature and salinity profiles from both models closest to the CTD station locations. We found generally good agreement between daily averaged model data and the measured short-term snapshots of temperature and salinity properties in all sampling years (Figures 8–10). There are also some notable differences between modelled and observed water mass properties. In 2008 at area C, for example, both models failed to accurately reproduce the pronounced thermocline and halocline in the upper 150 m of the water column, as well as the occasionally very high salinities of up to 36 (Figure 8). Furthermore, additional differences could be attributed to the space-time bias between the CTD point measurements and model data representing conditions inside an entire grid cell, as well as the intrinsic variability in the CTD data from near-surface processes and partial tidal signals that are not resolved by the time-averaged model data. In summary, there is a good agreement between modelled and observed water mass properties that represent a more stable steady state in contrast to short-term variability that can be attributed to short-term changes in near-surface processes and partially resolved tidal signals.

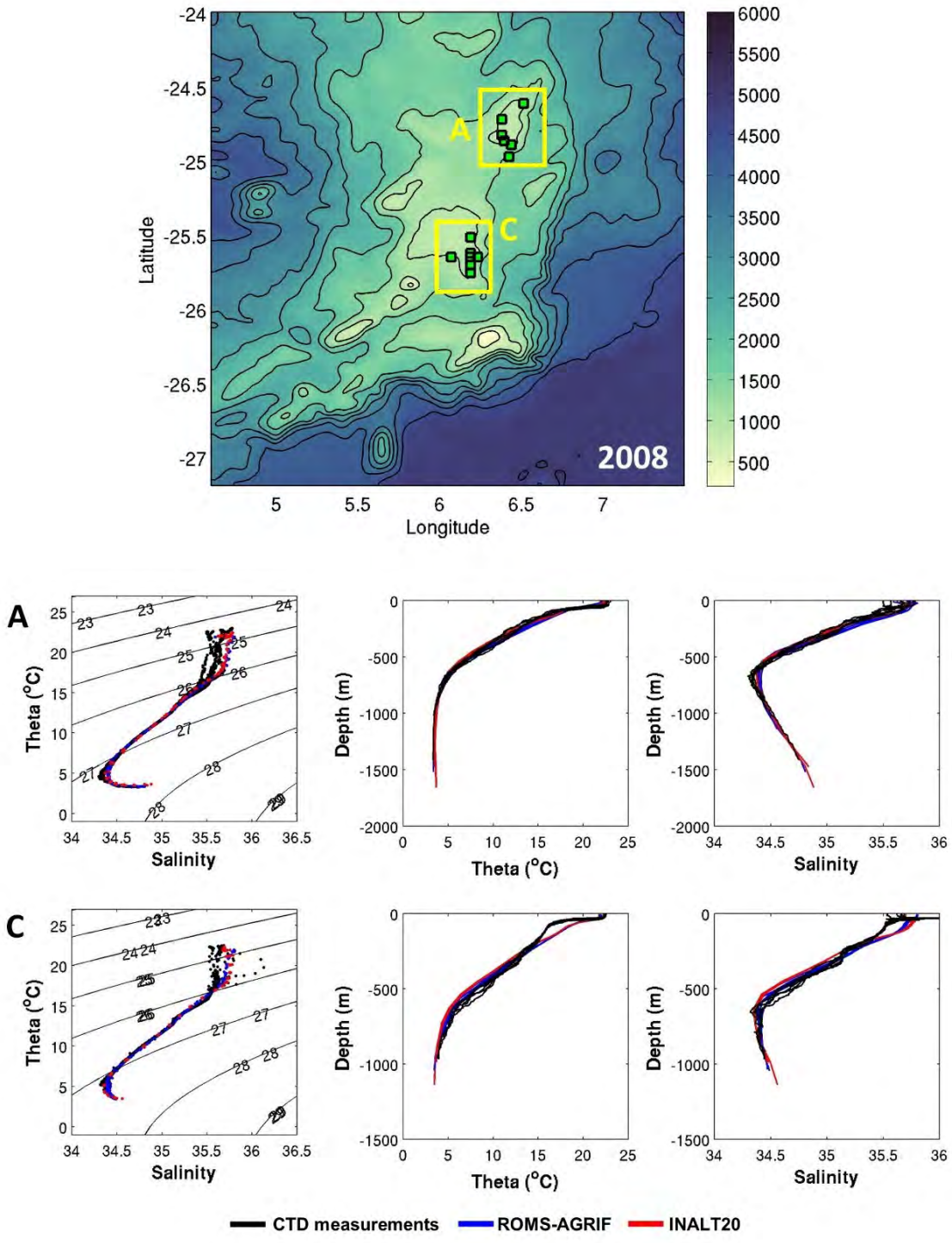

Figure 8. Observed vs modelled water mass properties pressure (dbar), potential temperature (°C) and salinity for CTD measurements obtained in 2008 at Valdivia Bank in sub-regions A and C (see also Figures 5 and 7). The individual sub-plots show T-S diagrams and depth profiles of potential temperature and salinity, respectively.

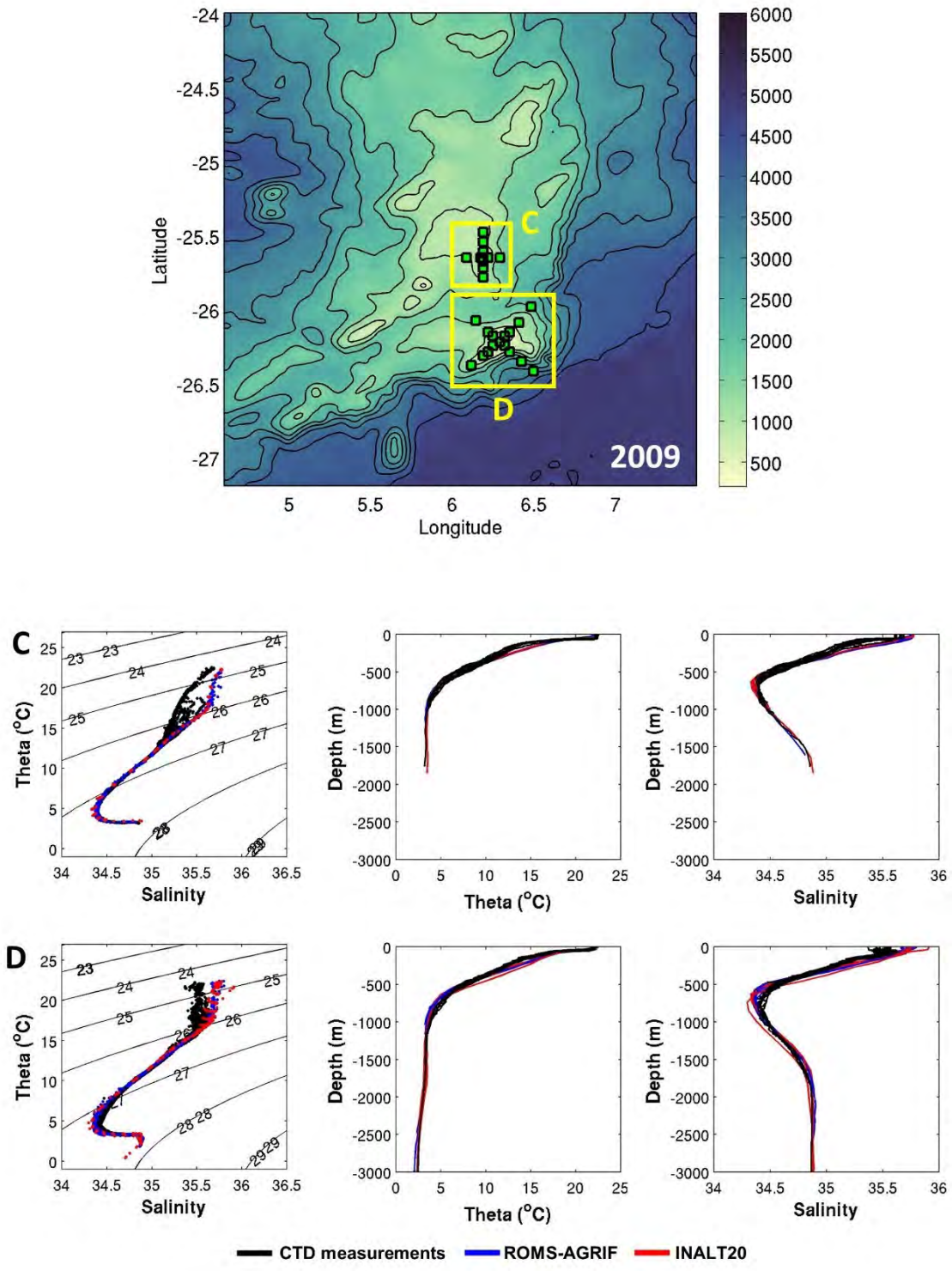

Figure 9. Observed vs modelled water mass properties pressure (dbar), potential temperature (°C) and salinity for CTD measurements obtained in 2009 at Valdivia Bank in sub-regions C and D (see also Figure 5 and 7). The individual sub-plots show T-S diagrams and depth profiles of potential temperature and salinity, respectively.

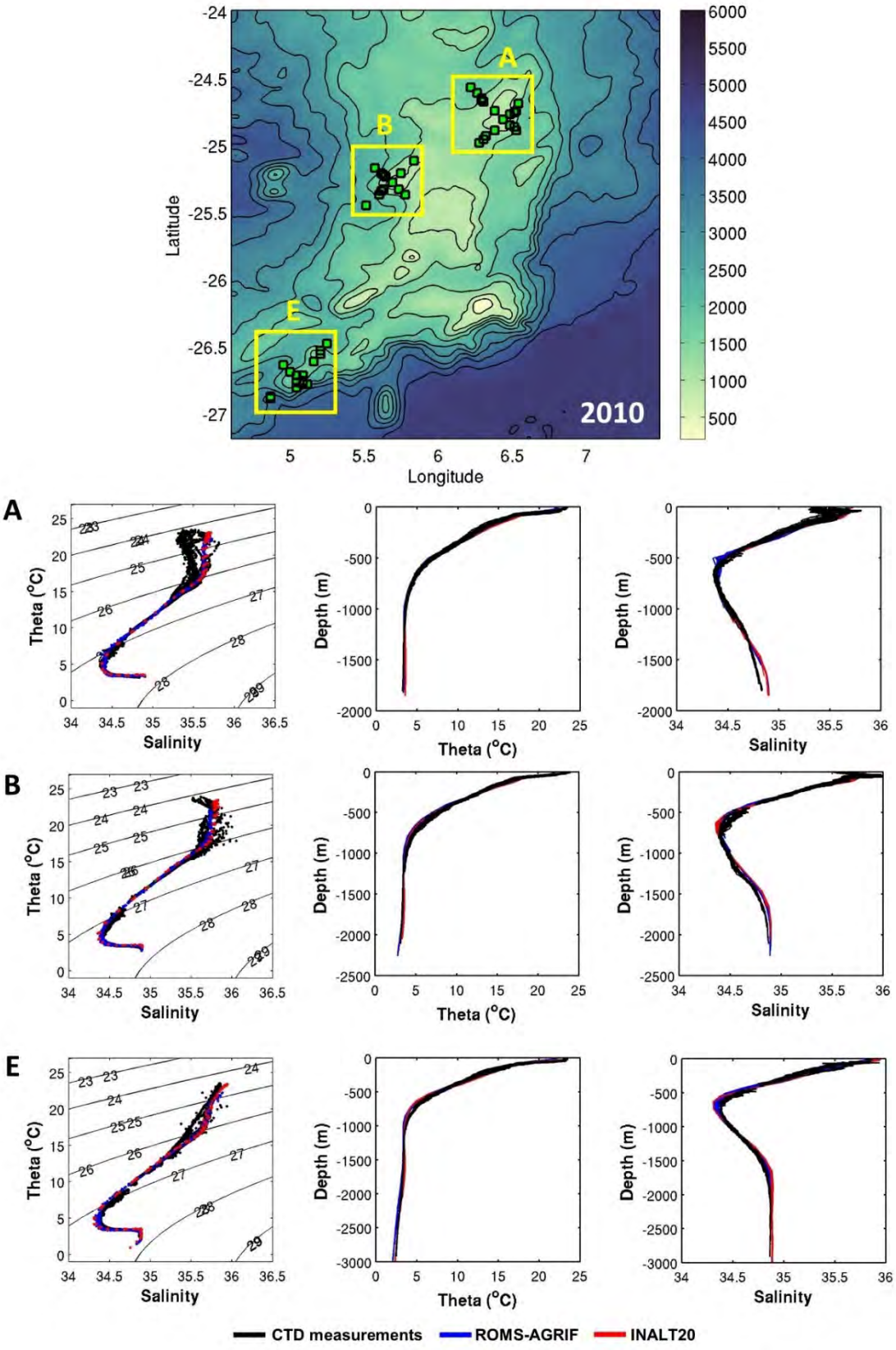

Figure 10. Observed vs modelled water mass properties pressure (dbar), potential temperature (°C) and salinity for CTD measurements obtained in 2010 at Valdivia Bank in sub-regions A, B and E (see also Figures 5 and 7). The individual sub-plots show T-S diagrams and depth profiles of potential temperature and salinity, respectively.

Near-bottom Currents and Water Mass Properties

Larger-scale circulation (parent grid)

The modelled near-bottom currents in the larger Valdivia Bank region show a complicated structure following multiple changes of the seafloor landscape along and across shallow seamounts and enclosed or semi-enclosed basins that merge into the deep-sea long steep slopes (Figure 11). The strongest bottom currents are predicted along the deep slopes to the east of the Valdivia Bank complex inside a northward flowing slope current with mean current speeds of 10–12 cm s^{-1}, as well as inside a narrow passage in the southwestern part of Valdivia Bank with mean current speeds of 0.25 m s^{-1} (Figure 11b). The near-bottom circulation at the bank is largely constrained by the size and shape of the shallower topographic elevations. The most prominent flow feature attached to topography on the Valdivia Bank is a time-mean anticyclonic (counter-clockwise) and largely symmetric recirculation along the slopes of the largest summit atop Valdivia Bank with current speeds of 6–8 cm s^{-1} (see currents inside the grey rectangle in Figure 11b).

In the wider Ewing Seamount area, the model results again show a focussing of near-bottom currents along steeper topographic gradients. The deep near-bottom circulation is dominated by a northeastward flow along the Walvis Ridge in the northwestern Cape Basin with maximum 3-year mean velocities not exceeding 6 cm s^{-1} and a southwestward return flow above the Walvis Ridge of magnitude 5–7 cm s^{-1} (Figure 12b). Mean near-bottom currents in the deep northern Cape Basin (eastern boundary of the model area) and outside the immediate Ewing Seamount area also show a predominantly northward flow with an occasionally meandering structure at magnitudes of 1–3 cm s^{-1}. Currents at Ewing Seamount (inside grey rectangle in Figure 12b) are largely anti-cyclonic and oriented along-slope along the deeper slopes with components of cross-isobath flow above the seamount summit. Maximum time-mean currents at Ewing Seamount were of magnitude 5 cm s^{-1}.

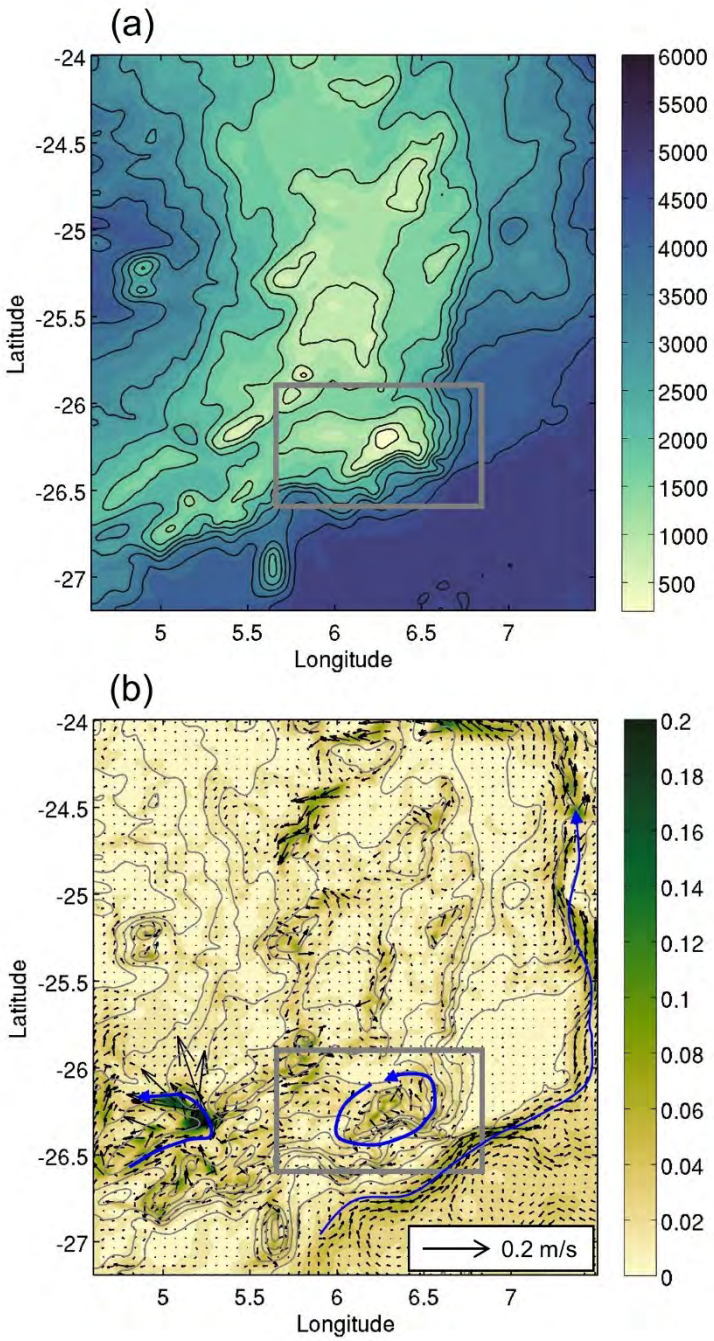

Figure 11. Composite of the time-mean near-bottom circulation in the larger Valdivia Bank region simulated for the years 2008–2010 with the ROMS-AGRIF Valdivia Bank parent grid setup (1,500 m resolution). (a) Model topography, (b) mean current speed and direction. Coloured contours indicate water depth in m (a) and current speed in m s^{-1} (b). Black contour lines in (a) and (b) show depth contours from 500 to 5,000 m at 500 m intervals. In (b) every 4th current vector is shown for improved clarity. Grey rectangles indicate the location of the child grid. Blue arrows highlight the major circulation features.

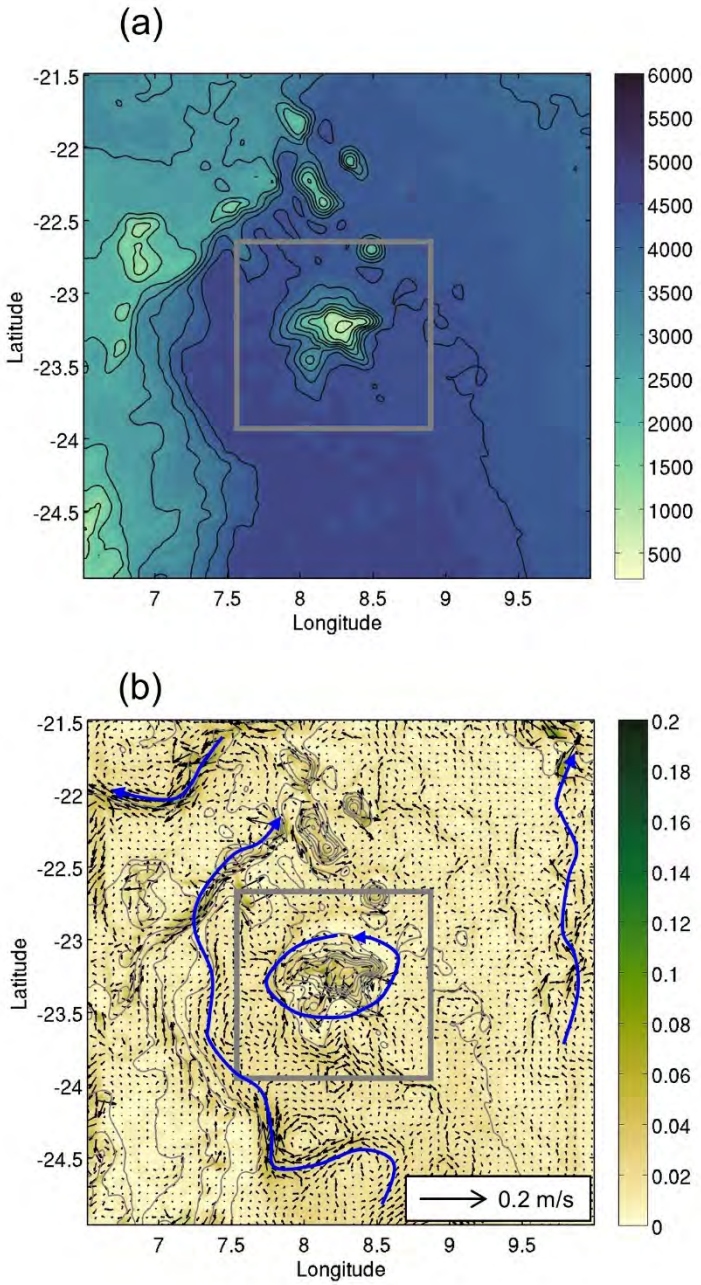

Figure 12. Composite of the time-mean near-bottom circulation in the larger Ewing Seamount region simulated for the years 2008–2010 with the ROMS-AGRIF Ewing Seamount parent grid setup (1,500 m resolution). (a) Model topography, (b) mean current speed and direction. Coloured contours indicate water depth in m (a) and current speed in m s^{-1} (b). Black contour lines in (a) and (b) show depth contours from 500 to 5,000 m at 500 m intervals. In (b) every 4th current vector is shown for improved clarity. Grey rectangles indicate the location of the child grid. Blue arrows highlight the major circulation features.

Local circulation patterns and water mass properties (child grid)

A more detailed view of near-bottom currents at Valdivia Bank and Ewing Seamount is presented based on results from the ROMS-AGRIF child grid simulations with improved bathymetry and spatial resolution (Figure 13, 14). At the Valdivia Bank central summit, mean bottom currents averaged over the years 2008–2010 at 500 m resolution show again the counter-clockwise recirculation along the summit slopes in combination with pronounced cross-slope currents above the summit. The strongest along-slope

mean current speeds were 6 cm s^{-1}, whereas cross-slope flows atop the summit were intensified up to 10 cm s^{-1} (Figure 13a). Rose diagrams of near-bottom currents at selected locations along the summit slopes confirm the presence of a stable and rectified along-slope anticyclonic flow with little variability in direction and only occasional periods of weakening and larger changes in flow direction or flow reversal during the entire simulation period. In contrast, the model predicts tidally dominated across-slope variations with corresponding periodic changes of flow direction atop the summit (Figure 13b).

Modelled annual time series of near-bottom water mass properties and currents at three different central summit locations (summit top, northern slope, southern slope) illustrate the temporal evolution and range of variability of potential temperature θ (° C), salinity S and current speed U (m s^{-1}) (Figure 14). Temperature and salinity variations largely follow a seasonal cycle superimposed on a pronounced spring-neap tidal cycle. Interannual changes are most pronounced at the shallower summit top (240 m) and dominated by strong excursions in temperature and salinity in 2008 with warmer and more saline water (southern hemisphere summer) or colder and less saline water (spring) when compared to other simulated years. At greater depths, interannual variations along the northern and southern slopes (approximately 740 m) are smaller, except for the 2008 southern hemisphere summer and spring 2008 events. Variations in current speed are in the range 1–8 cm s^{-1} and are dominated by the spring-neap tidal cycle with some seasonal modulation, which almost never exceeds the fortnightly tidal current speed maximum, except for occasional events of intensified flows. Such strongly intensified currents at the summit top and along the deeper slopes reach magnitudes up to 15 cm s^{-1} and can likely be attributed to enhanced mesoscale far field variability propagating into the central summit area, although a corresponding imprint in temperature and salinity is only occasionally recognisable.

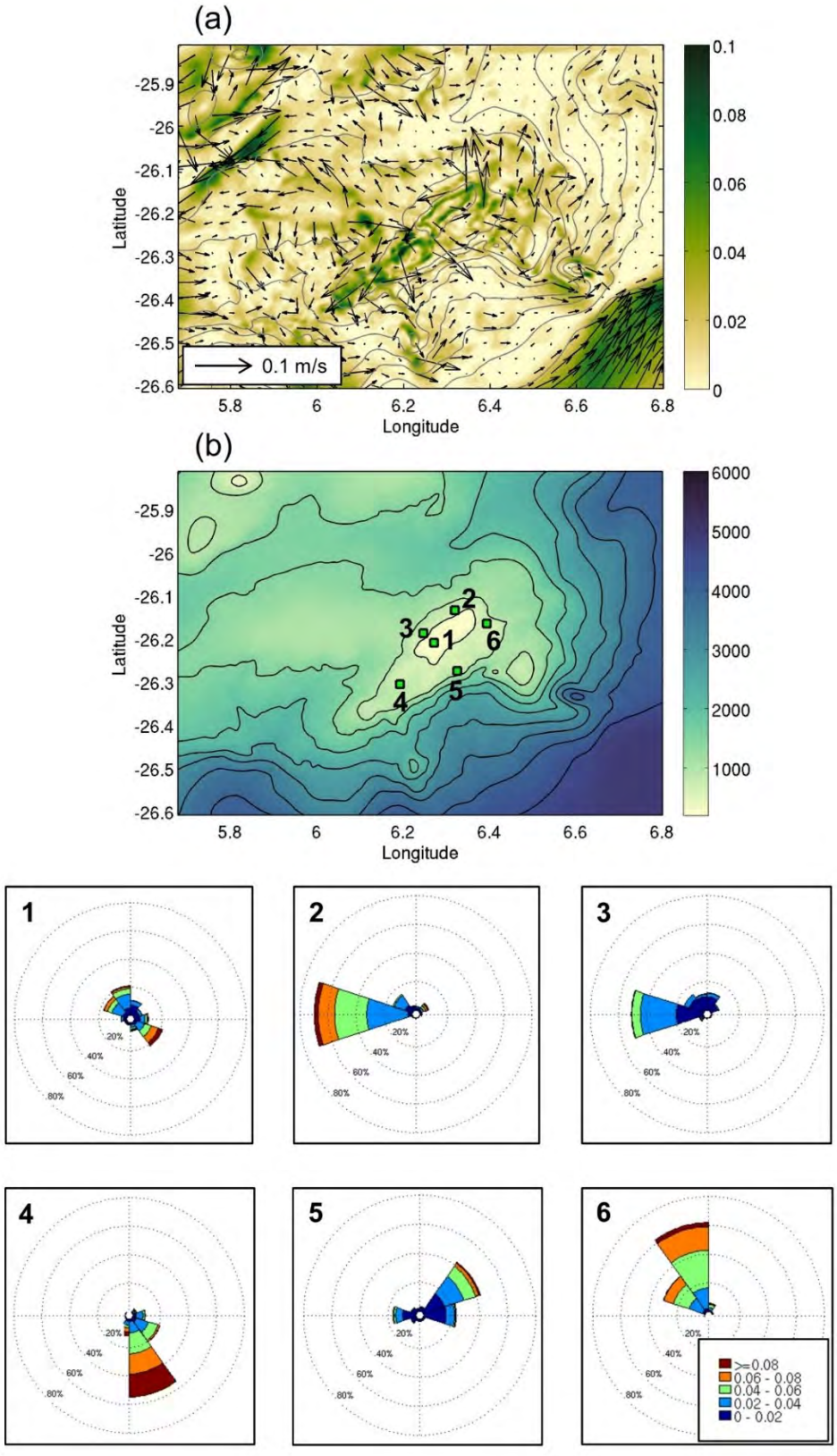

Figure 13. (a) Time-mean near-bottom circulation at the central Valdivia Bank summit simulated from 2008–2010 with the ROMS-AGRIF Valdivia child grid (500 m resolution). (a) Mean current speed and direction (m s^{-1}), (b) model topography and rose diagrams calculated from daily averaged modelled current velocities. In (a) every 8th current vector is shown for better clarity.

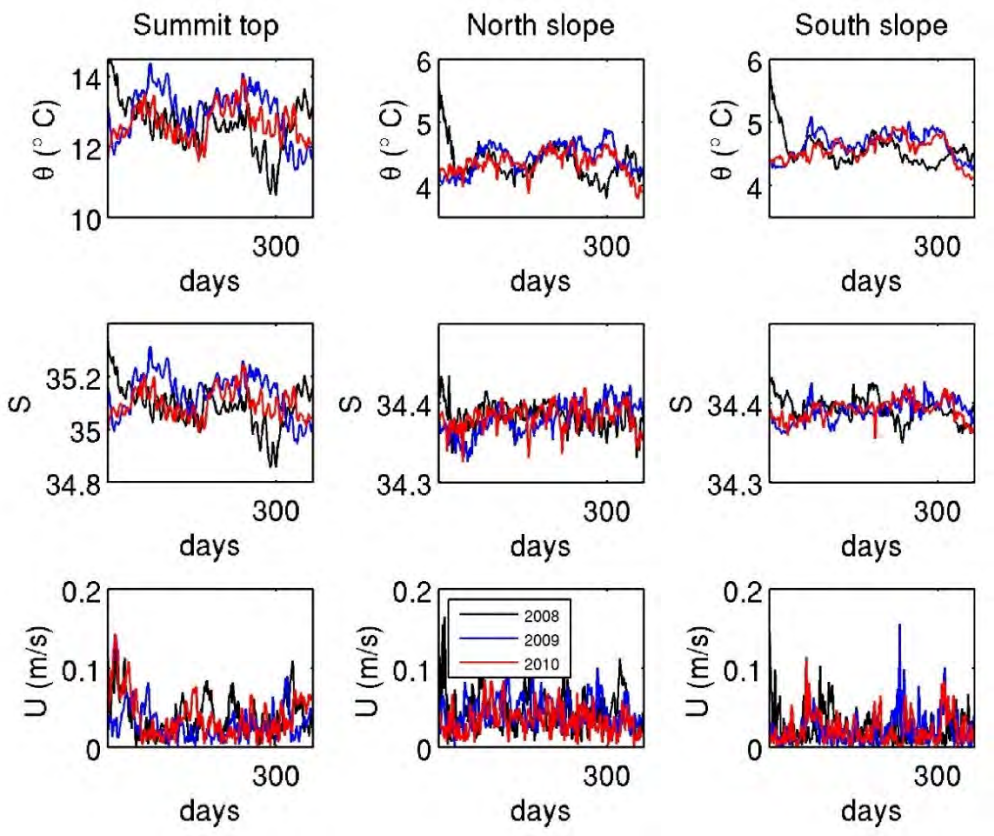

Figure 14. Modelled time series of potential temperature θ (°C), salinity S and current speed U (m s^{-1}) at three locations at the central Valdiva Bank summit. Locations refer to the summit top (240 m, position 1 in Figure 14b), north slope (740 m, position 2 in Figure 14b), and south slope (740 m, position 5 in Figure 14b).

At Ewing Seamount the model predicts a mean circulation pattern similar to central Valdivia Bank with largely along-slope flow along the upper seamount slopes (1,100–1,300 m) and cross-slope flow atop the summit (Figure 15a). However, flow rectification along the slopes is less pronounced than at Valdivia Bank. Rose diagrams of Ewing Seamount currents show that currents in this depth range (with currents at 1,250 m and 12,280 m depth shown as an example in Figure 15b) are still aligned in a counterclockwise sense but reveal longer periods of variability in magnitude and direction when compared to central Valdivia Bank. Current velocities along the upper flanks show a typical range of 2–5 cm s^{-1} and only occasionally exceed 6 cm s^{-1}. In contrast to central Valdivia Bank, modelled currents atop the Ewing Seamount summit are frequently rectified and aligned in a southwestward direction with maximum velocities in the range 6–10 cm s^{-1} (Figure 15b).

The strong contrast in current magnitude between seamount summit and upper slopes can also be seen in timeseries at individual locations and is a recurring feature in all years. Modelled upper slope currents with magnitudes 2–5 cm s^{-1} dominate throughout most of the year in the depth range 1,250–1,280 m with small fortnightly tidal modulation and only occasionally and short-term (< 20 days) intensified flows of magnitude larger than 8–10 cm s^{-1} (Figure 16). Atop the summit, current magnitudes are consistently enhanced and typically twice as high as along the upper flanks (Figure 16). Temporal variations in temperature and salinity are again largely determined by the seasonal cycle with larger interannual variability atop the summit during the simulation period, but smaller changes between model years along the upper slopes (Figure 16).

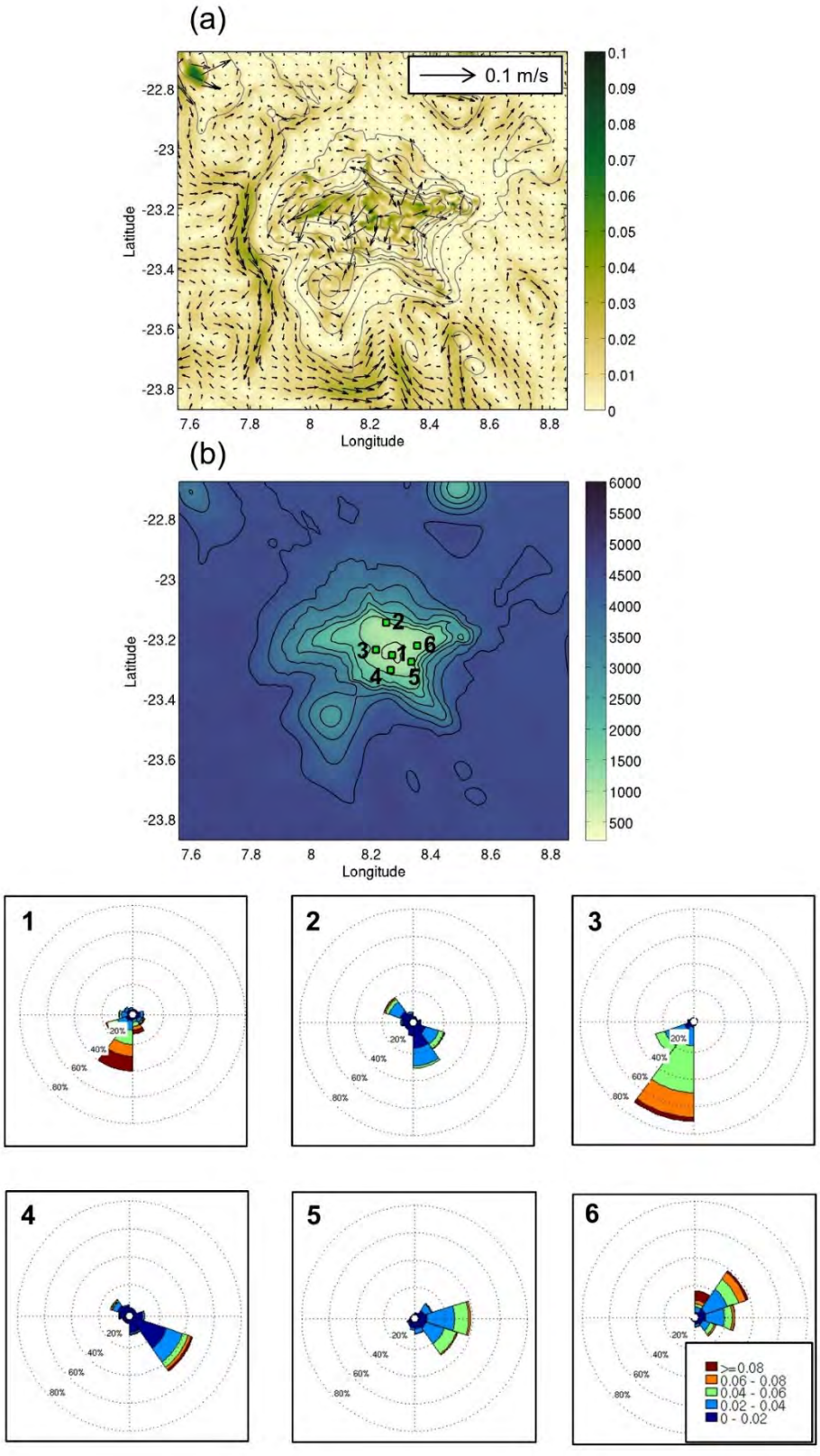

Figure 15. (a) Time-mean near-bottom circulation at Ewing Seamount simulated from 2008–2010 with the ROMS-AGRIF Valdivia child grid (500 m resolution). (a) Mean current speed and direction (m s^{-1}), (b) model topography and rose diagrams calculated from daily averaged modelled current velocities. In (a) every 8^{th} current vector is shown for better clarity.

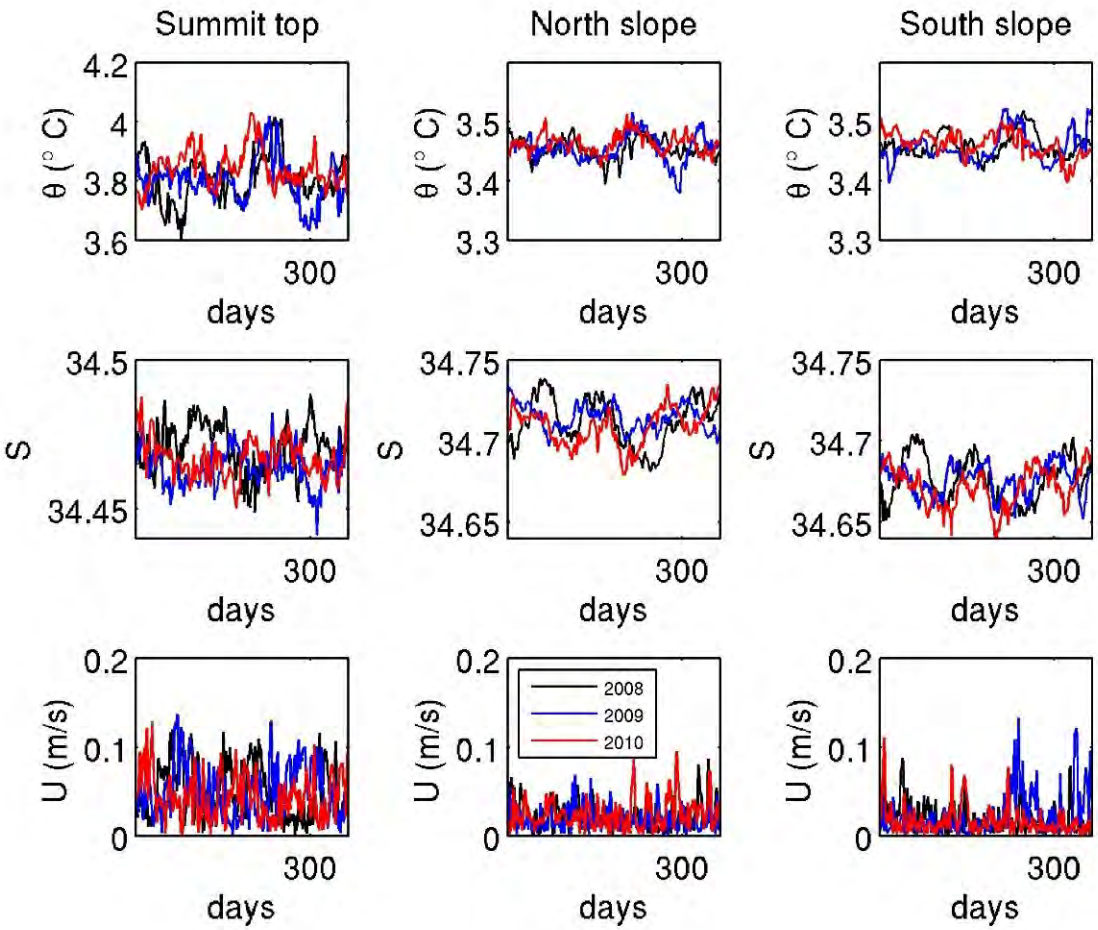

Figure 16. Modelled time series of potential temperature θ (°C), salinity S and current speed U (m s^{-1}) at three locations around the Ewing Seamount summit. Locations refer to the summit top (850 m, position 1 in Figure 16b), north slope (1,250 m, position 2 in Figure 16b), and south slope (1,280 m, position 4 in Figure 16b).

Benthic dynamics and biophysical connections

In this analysis, we aimed at developing a better understanding of physical drivers of larval transport patterns in the Valdivia Bank area. To achieve this, we compare modelled water mass properties, dynamic variables, and physical mechanisms with observed occurrence (presence and statistical randomly selected pseudo-absence) of benthic filter and suspension feeding organisms. We used observed occurrences of sessile Cnidaria and Porifera species as an example, which were obtained from benthic samples collected during the 2008–2010 RAP-SUR surveys (López Abellán and Holtzhausen, 2011). The role of currents for supplying and replenishing sessile benthic communities with organic matter and other food sources has been highlighted in a large number of studies (e.g., Mienis et al., 2007; Khripounoff et al., 2014; de Froe et al., 2022). Food supply is thought to be directly related to hydrodynamics (e.g., through variability and strength of local and far-field currents, local mixing and turbulence), bringing food particles in direct contact with the benthic organisms. The capacity to predict benthic species distribution includes knowledge of functional relationships between ecosystem components and changes in physical and hydrochemical water properties over space and time but may also consider the role of physical processes and mechanisms that drive food supply (Mohn et al., 2023). Here we tested how well distributions of modelled properties relate to near-bottom currents (mean and maximum current speed) and different functional descriptors of food supply (kinetic energy dissipation,

internal wave slope criticality) matched the distribution of benthic Cnidaria and Porifera communities at Valdivia Bank. Kinetic energy dissipation describes topographically enhanced transfer of kinetic energy and conversion towards higher frequency motions (Nikurashin et al., 2013), which has large importance for sessile benthic organisms as a mechanism of supply and re-distribution of food particles. Kinetic energy dissipation rates are estimated from daily averages of the modelled 3D velocity field expressed as in Table 3. Internal tides in the interior ocean are generated through the interaction of the barotropic tide with topographic slopes at seamounts, ridges, canyons and other abrupt topographic elevations. The steepness of the topographic slope compared to the angle of the internal tidal wave is an important parameter determining the strength of internal tide generation (Cacchione et al., 2002). The topographic slope (h) is considered critical or near-critical when its steepness matches or is close to the steepness of the internal wave beam angle (c). At critical slopes, the internal tide resonates, and vertical mixing is intensified. At gentler subcritical slopes (h<c), internal waves pass the topographic slope without significant interference. At steeper supercritical slopes (h>c), internal waves are reflected and can advect food particles over larger distances (see Table 3 for the formulation of internal wave slope criticality).

Table 3. Description of parameters and functional proxies used in the assessment of physical drivers of benthic species distribution patterns.

Parameter	Description
U_{mean} (m s^{-1})	Mean current speed from daily averaged model output of velocity components u, v (parent grid, 1,500 m resolution) and calculated as $U = \sqrt{u^2 + v^2}$.
U_{max} (m s^{-1})	Maximum current speed at each grid point from daily averaged model output of velocity components u, v (parent grid, 1,500 m resolution) and calculated as $U = \sqrt{u^2 + v^2}$.
$\varepsilon = \rho \cdot A_h \left[\left(\frac{\partial U}{\partial x}\right) \cdot \left(\frac{\partial U}{\partial x}\right) + \left(\frac{\partial U}{\partial y}\right) \cdot \left(\frac{\partial U}{\partial y}\right)\right] + \rho \cdot A_v \left[\left(\frac{\partial U}{\partial z}\right) \cdot \left(\frac{\partial U}{\partial z}\right)\right]$	Kinetic energy dissipation rates from daily averaged model output of the modelled 3D velocity field (Nikurashin et al. (2013). The horizontal viscosity $A_h = 1\ m^2 s^{-1}$ and vertical viscosity $A_v = 10^{-3}\ m^2 s^{-1}$ consider the large aspect ratio between horizontal and vertical exchange of momentum. The density of seawater ρ (kg m^{-3}) is calculated from the modelled temperature and salinity fields.
S = h / c	Internal wave slope criticality (St Laurent and Garrett, 2002; Cacchione et al., 2002). The topographic slope h is calculated from the model topography (parent grid, 1,500 m resolution). The internal wave slope is calculated as $c = \sqrt{\frac{\omega^2 - f^2}{N^2 - \omega^2}}$, with tidal frequency ω =1.4053e-4 s^{-1} (M_2 tidal component) and inertial frequency f.

Mean and maximum current speed

As a first step to estimate possible bio-physical connections we mapped benthos presence data on near-bottom currents from the 2008–2010 model simulations. Figure 17 shows the time-averaged and maximum near-bottom current speeds from the parent grid simulations (1,500 m resolution) superimposed on all Cnidaria and Porifera presence data sampled from 2008–2010. Maximum near-

bottom current speeds represent the maximum value at each model grid point over the entire simulation period based on daily averaged model output. Observed Cnidaria and Porifera occurrences exist over a limited range of modelled mean currents speeds of 2–7 cm s^{-1} but extend over a larger range of instantaneous maximum current speeds of 10–30 cm s^{-1}. Larger aggregations of Cnidaria and Porifera occurrences do not seem to show preference for a dynamic regime defined by a characteristic and specific range of flow magnitudes.

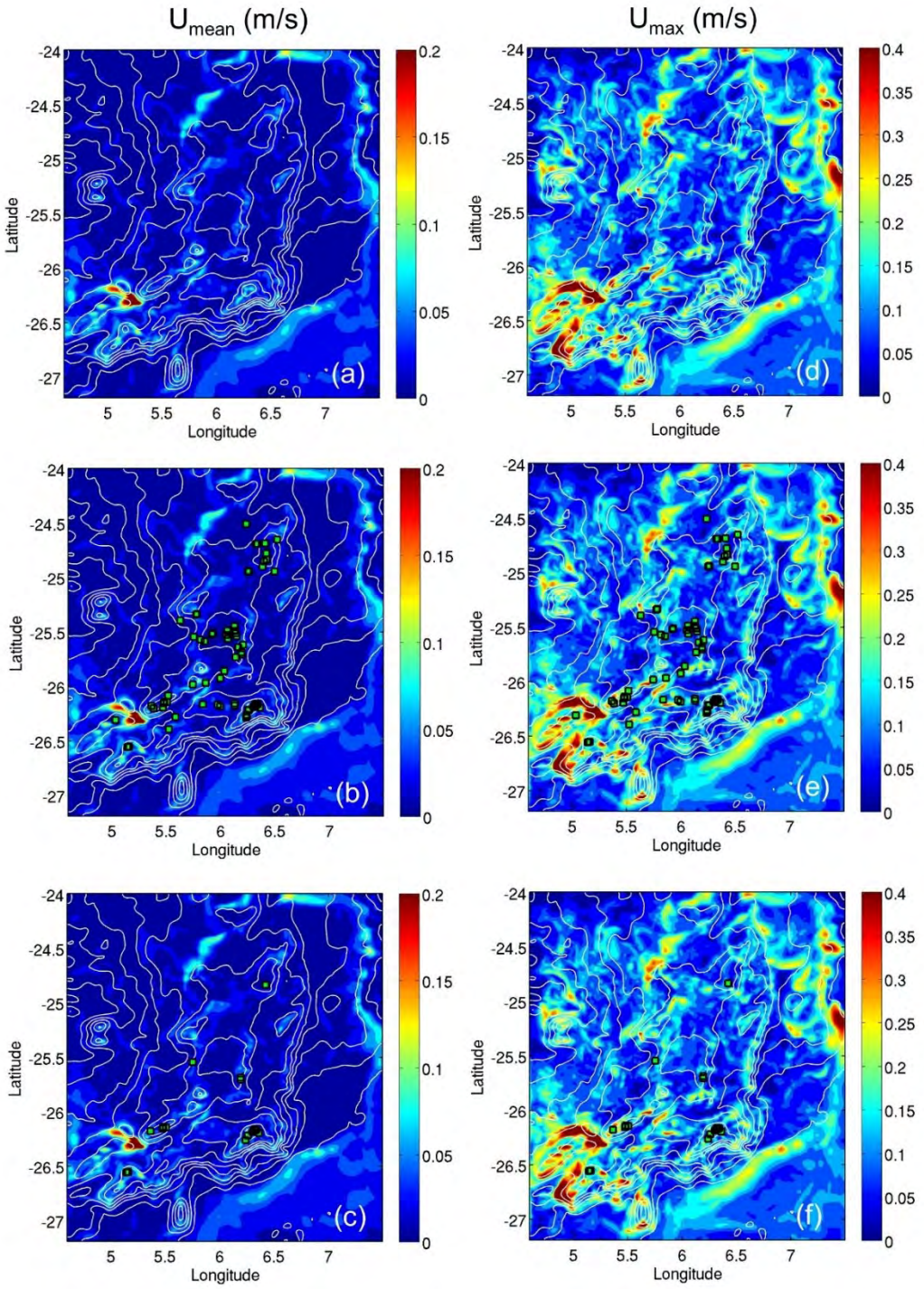

Figure 17. Mean and maximum currents speeds (a, d) calculated from daily averaged model output of the 2008–2010 Valdivia Bank parent grid simulations. Mean and maximum current speeds are superimposed on observed

distributions of Cnidaria in (b, e) and Porifera in (c, f) respectively. White contour lines represent depth contours at 500 m intervals in the range 500–6,000 m.

Kinetic energy dissipation

Near-bottom distributions of rates of kinetic energy dissipation (ε) at Valdivia Bank are presented in Figure 18. Mean (2008–2010) kinetic energy dissipation is enhanced above most of the Valdivia Bank complex when compared to surrounding deep waters. Local maxima in ε can be found above the central bank summit to the Southeast and in the southwestern corner of the bank intersected by a narrow passage (Figure 18a). Elevated levels of ε are also visible across other areas of the Valdivia Bank complex with enhanced horizontal gradients in the topographic slopes and near-bottom velocity field. Kinetic energy dissipation rates in these areas are one to two orders of magnitudes higher than modelled dissipation rates outside the immediate Valdivia Bank area (Figure 18a). Our model results indicate that locations of enhanced kinetic energy dissipation rates correspond well with observed distributions of Cnidaria and Porifera occurrences. Larger aggregations of Cnidaria and Porifera seem to be connected with areas of intensified energy dissipation but can almost never be found in bank areas with low levels of ε (< 9 $\log_{10}(\varepsilon)$ W kg^{-1}). An interesting exception, however, can be found for Cnidaria in some troughs (e.g., at 25.5 °S, 6 °E), where Cnidaria assemblages exist in an environment with current speeds and weaker kinetic energy dissipation. Whereas mean and maximum bottom current speed are descriptive variables and their connection to the presence of benthic species may not always be conclusive, it seems that combining properties with more functional descriptors such as kinetic energy dissipation provides a more conclusive picture: larger aggregations of Cnidaria and Porifera occurrences seem to be often connected with areas of intensified kinetic energy dissipation.

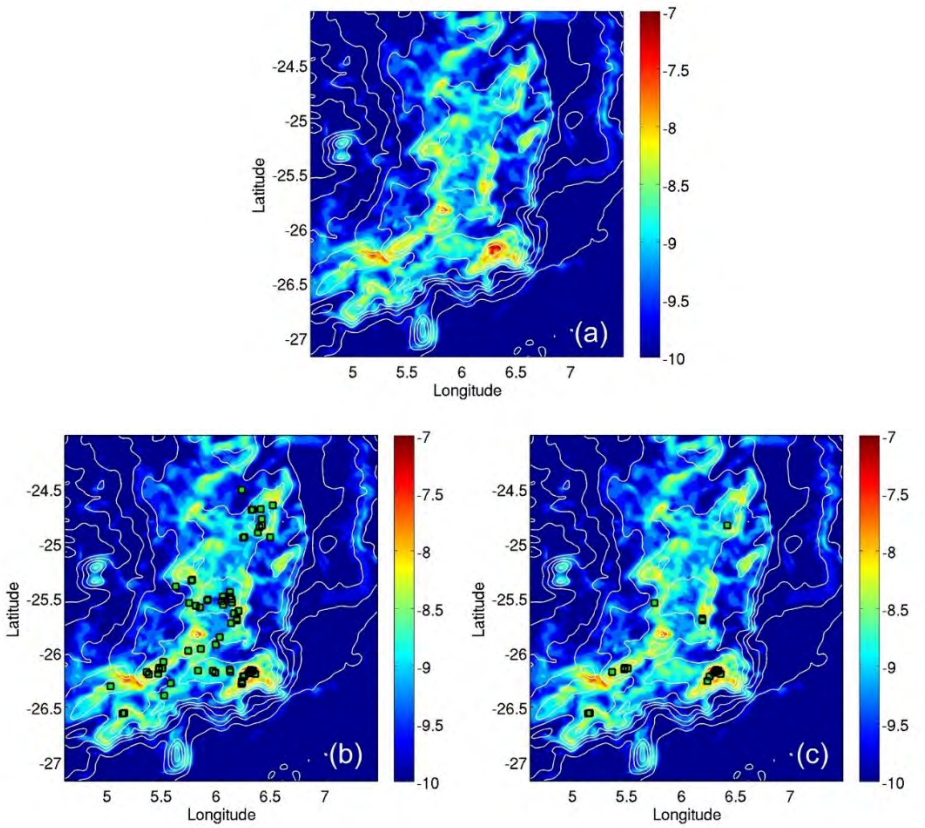

Figure 18. Mean near-bottom kinetic energy dissipation rate log10(ε) (W kg^{-1}) calculated from daily averaged model output of the 2008–2010 Valdivia Bank parent grid simulations. Kinetic energy dissipation rates are

superimposed on observed distributions of Cnidaria in (b) and Porifera in (c) respectively. White contour lines represent depth contours at 500 m intervals in the range 500–6,000 m.

Internal wave slope criticality

Calculations of S=h/c were made using daily averaged model output for the years 2008–2010. Bottom gradients h computed from the 1,500 m model topography variations in the x (longitude) and y (latitude) directions were averaged over each 1,500 x 1,500 m grid cell. The estimates for the internal wave slope steepness c were based on three-year averages for the modelled near-bottom buoyancy frequency N and the frequency of the dominant M2 semi-diurnal tidal constituent. Topographic slopes are critical or near-critical (S≈1) in areas with the highest bottom velocities. This includes the region connected to the narrow passage in the Southwest of the Valdivia Bank complex and the steep slopes connecting the bank to the surrounding deep sea (Figure 19a). Over most of the Valdivia Bank complex, topographic slopes are near-critical or super-critical (S>1). Areas with gentle topographic slopes (S<1) mainly exist throughout the northern Valdivia Bank complex and are sub-critical (transmissive) with respect to the interaction with internal waves. Observed occurrences of benthic communities are mostly linked to critical or supercritical slopes, again with the exception of aggregated Cnidaria occurrences in the central Valdivia Bank trough (Figure 19b, c).

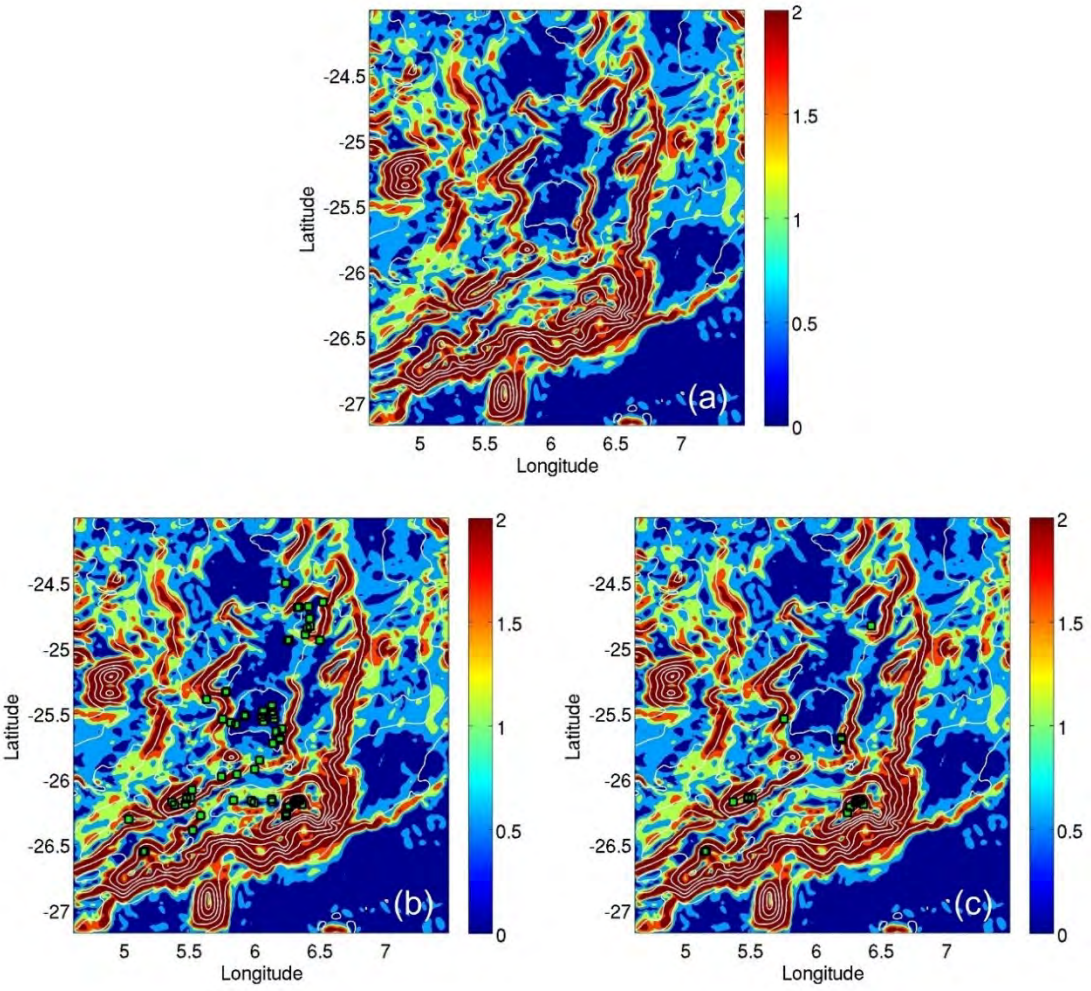

Figure 19. Mean values of internal wave slope criticality S calculated from daily averaged model output of the 2008–2010 Valdivia Bank parent grid simulations. The values of S are superimposed on observed distributions of Cnidaria in (b) and Porifera in (c) respectively. The values of S correspond to critical or near-critical (S≈1), sub-

critical (S<1) and supercritical slopes (S>1) respectively. White contour lines represent depth contours at 500 m intervals in the range 500–6,000 m.

Environmental conditions at species presence and random pseudo absence locations

A more detailed assessment of modelled environmental conditions at observed Cnidaria and Porifera occurrences (presence data) is presented in the following section as a comparison of observed occurrences (presence data) with model data at random access pseudo absence locations. Pseudo-absences (sometimes also defined as environmental background data) are not considered as true absences, but rather represent the available environment in the studied area outside the observed species presence data (Barbet-Massin et al., 2012). Cnidaria and Porifera presence data were obtained from the 2008–2010 RAP-SUR project dataset (López Abellán and Holtzhausen, 2011). Corresponding presence locations for modelled environmental parameters were approximated by calculating the positions of the model grid points, which are located closest to the locations of the observed data. In a second step, pseudo absence locations were calculated from model data in areas outside presence locations using an equal number of randomly selected positions. The resulting analysis is shown in Figure 20 for Cnidaria and Figure 21 for Porifera communities. Cnidaria and Porifera communities exist in waters with a median temperature θ = 4-5 °C and a median salinity S = 34.5-34.6. Conditions in random pseudo absence locations were generally lower in temperature, but higher in salinity. It should be noted, however, that there exists a significant depth bias in connection with the large depth range covered by the benthic communities extending from 270 to > 1,000 m. Benthic occurrences of both phyla are bathed in waters of higher mean and maximum speeds than predicted for random absence locations. The median (maximum) current speed at presence locations is 3.5–5 (15–20) cm s^{-1}, whereas median (maximum) currents at absence locations do not exceed 2 (10) cm s^{-1}. The distribution of Cnidaria and Porifera across the Valdivia Bank is connected mostly with critical or supercritical slopes with a median at S ≈ 1 indicating critical slopes, whereas absence locations largely fall in the median subcritical category, however with a large spreading of values. There exists a distinct difference in kinetic energy dissipation rates ε between presence and random absence locations for both phyla. ε values at presence locations are 1–2 orders of magnitude larger than dissipation rates at random absence locations. The combination of enhanced kinetic energy dissipation rates and critical slopes generates a dynamic environment with large potential of redistributing organic material and increasing food items available to the benthic communities. Our evaluation suggests that these areas are the preferred environment for coral and sponge communities in the Valdivia Bank region.

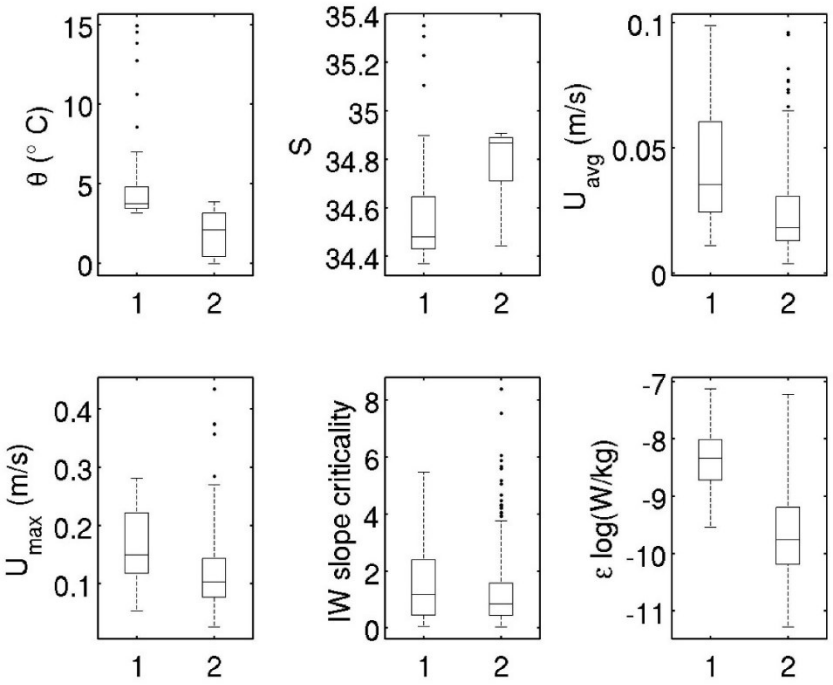

Figure 20. Box plots of near-bottom temperature θ (° C), salinity S, time-mean current speed U_{avg} (m s^{-1}), maximum current speed U_{max} (m s^{-1}), internal wave slope criticality and kinetic energy dissipation $\log_{10}$ (ε) (W kg^{-1}) at observed Cnidaria presence (1) and randomly selected (pseudo) absence locations (2) at Valdivia Bank. Black bars in the centre represent the median. Black boxes represent the 25 and 75% quartiles. Whiskers extend two times the interquartile range indicating the spreading of values from minimum to maximum across the interquartile.

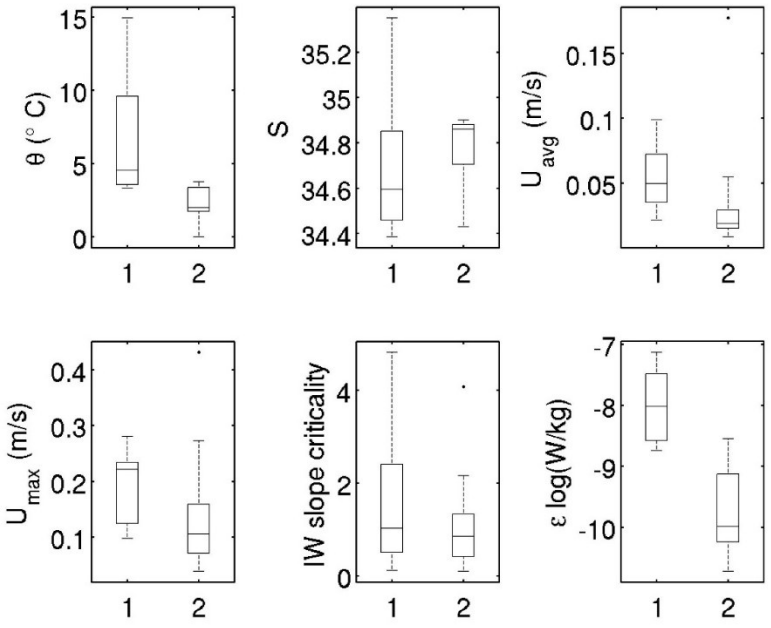

Figure 21. Box plots of near-bottom temperature θ (° C), salinity S, time-mean current speed U_{avg} (m s^{-1}), maximum current speed U_{max} (m s^{-1}), internal wave slope criticality and kinetic energy dissipation $\log_{10}$ (ε) (W kg^{-1}) at observed Porifera presence (1) and randomly selected (pseudo) absence locations (2) at Valdivia Bank. Black bars in the centre represent the median. Black boxes represent the 25 and 75% quartiles. Whiskers extend two times the interquartile range indicating the spreading of values from minimum to maximum across the interquartile.

Some comments on conceptual limitations

Our approach of introducing physical processes as functional descriptors of benthic species communities also bears conceptual limitations. We used time-mean (long-term) averages of kinetic energy dissipation rates ε and internal wave slope criticality S to link observed benthos occurrences and random pseudo-absence locations to different dynamic environments. Using long-term averages of S, however, may lead to misinterpretations of biophysical connections. For example, S defines regimes with qualitatively different dynamics (subcritical, critical, supercritical). If benthic organisms tend to avoid the most turbulent environments, they may be present at sub- and supercritical slopes, but not at critical or near-critical slopes. In such conditions, calculating averages of S would give values close to one (near-critical), which would not be representative of typical conditions attractive to these organisms. Moreover, we did not consider temporal changes on seasonal and interannual timescales in internal wave slope criticality. However, it has been shown that seasonal changes in near-bottom stratification may cause significant changes in internal tide characteristics and dynamics (Cacchione et al., 2002).

1.5. Discussion

Cold-water corals and sponges are VME indicators providing important ecosystem services and have high conservation value (e.g., Armstrong et al., 2014). Yet, we still only have scattered knowledge about their global distribution and environmental drivers (Roberts and Cairns, 2014), and the South Atlantic is no exception (Bergstad et al., 2019a). An increasing number of cold-water coral and sponge ecosystems have been well explored recently providing a wealth of valuable data to feed local and basin-scale species distribution and habitat suitability models, and strongly improving our knowledge about their spatial distribution and temporal evolution (Davies and Guinotte, 2011; Knudby et al., 2013; Flögel et al., 2014; Morato et al., 2020; Sundahl et al., 2020). Observational and model studies have shown that local hydrodynamic hotspots and high advection rates of food particles are important drivers for the well-being of cold-water corals (Mienis et al., 2007; Soetaert et al., 2016; de Froe et al., 2022; Mohn et al., 2023). At such locations kinetic energy is converted from large-scale currents and barotropic tides to internal tides and enhanced turbulence and small-scale mixing over rough topography (Nikurashin et al., 2013) or kinetic energy is advected from the oceanic far field carrying larvae and food (Schulz et al., 2020). Well-tested hydrodynamic models in combination with in-situ sampling can resolve or partly resolve this energy cascade and thus can help to improve predictions of VME indicator species distribution at management scales of a few kilometres or less (Mohn et al., 2023). Dynamic downscaling resolves the 3-D velocity field at spatial scales that are relevant for larger cold water coral reefs and sponge assemblages in combination with high-resolution terrain data and accurate boundary conditions. Our model results from Valdivia Bank indicate that functional proxies calculated from modelled velocities and water mass properties can be a useful supplement to more traditional predictors such as terrain variables and scalar water mass properties. For example, enhanced kinetic energy dissipation rates and areas of internal wave generation and propagation appear to be closely linked to benthic species occurrence. Even though our models do not explicitly resolve non-linear processes such as turbulence and internal wave breaking, mechanistic predictors from our models can be useful proxies to identify locations where enhanced vertical mixing may occur and may connect hydrodynamics and benthic ecology.

In an ongoing collaboration between GEOMAR and Aarhus University, the particle entrainment and retention potential of the waters above Ewing Seamount, specifically the role of the utilised model

formulations in the INALT20 and ROMS-AGRIF models will be explored as part of Master Thesis project. Some spatially resolved data on geomorphology and biota were collected at individual cruises at the Valdivia and Ewing seamounts between 2008 and 2014 (Bergstad et al. 2019b, and references therein), but more detailed studies on particle connectivity at the seamounts are still lacking. Particle experiments with Ocean Parcels (Delandmeter and van Sebille, 2019) will be performed to test the exchange of water above Ewing Seamount with the surrounding deep ocean. Particle entrainment, retention and advective loss in relation to ocean currents will be described and quantified.

Chapter 2. Study Region 3: Hydrodynamics and properties of the hydrothermal plume at Lucky Strike

Cyrien Lemaréchal[1], Guillaume Roullet[1] and Jonathan Gula[1]

[1]Université de Bretagne Occidentale, CNRS, IRD, Ifremer, Laboratoire d'Océanographie Physique et Spatiale (LOPS), IUEM, Brest, France

2.1. Abstract

In contrast to Walvis Ridge, the task at Lucky Strike focussed on the vertical motion from injection at the vent to the neutral level, where the hydrothermal material is then dispersed horizontally. The vertical motion is due to the turbulent buoyant plume. To study this plume, we set up and analysed large eddy simulations (LES) with grid size down to 1 cm to resolve the outlet of a vent. We diagnosed essential variables of the plume: height, temperature profile, entrainment rate, mixing efficiency. Our results show that the plume of a single vent reaches 150 m, the height of the Lucky Strike vents field. This is contrary to a one-dimensional model that predicts an altitude of only a half. We show that the first metres of the plume, near the vent, are very special. The entrainment rate (0.04) is smaller than classically used, the mixing efficiency is very large (0.7), and the nonlinearity of the equation of state has a crucial effect on the vertical acceleration.

2.2. Introduction

In this work we aimed at studying the hydrodynamics at the ultra-high resolution (1 m to 100 m) to investigate energy dissipation, diapycnal mixing and transport of species near the seafloor. These scales are of direct interest for the biologists, the geochemists and the geophysicists who focus on a particular hydrothermal site. This work is a contribution to better understand and characterise the hydrodynamic context. At these scales the main process is the presence of buoyant plumes driven by the hot springs. The first metres of hydrothermal plumes are emblematic of hydrothermal sources, with a conic turbulent flow (Figure 22). These first metres are well observed by camera with hours of recording at many hydrothermal sites, and in particular at Lucky Strike (LS), the site chosen for this work. However, accurate measurements such as the vertical speed, temperatures profiles, or energy dissipation, are either seldom or non-existent, as it is still very difficult to perform measurements inside the plume. In addition, these first metres are only the tip of the plume. The plumes extend vertically over tens to hundreds of metres, depending on the site. At Lucky Strike the plume rises up to roughly 150 m above the sea floor, even though a recent study detects hydrothermal material up to 300 m in the water column (Artigue et al., 2022). As it rises vertically, the plume entrains surrounding cold water, making the plume wider and colder. The plume stops rising when its inner temperature reaches the ambient temperature, at the neutral buoyancy level. The basic phenomenology can be described by a one-dimensional model proposed by Morton et al. (1956), referred to as MTT in the following text. However, this model only provides a first order estimate of the plume characteristics. The aim of this work was to perform large eddy simulations (LES) to obtain more accurate plume properties at Lucky Strike (Figure 22a).

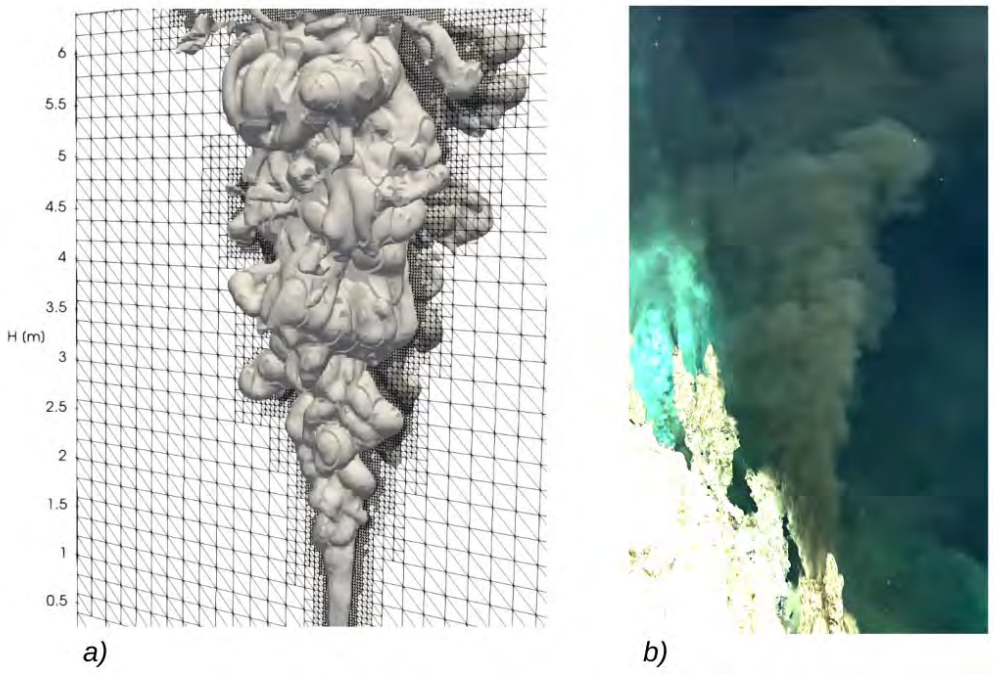

Figure 22. Qualitative view of the LES (a) compared to in situ video capture (b) of a plume at Lucky Strike.

2.3. Materials & Methods

We performed LES with the Basilisk code, an open-source code (Popinet, 2018). The plume is forced by imposing the temperature T and a vertical velocity w at the spring, modelled as an outlet of radius r, located a one metre above a flat bottom. The ambient stratification is linear in the vertical (constant Brunt Vaisala frequency N), with N=6.85 10^{-1} s^{-1}, determined from the observations at LS. At the outlet the ambient temperature is 4.5°C, while the hot water is at 300°C. We tested three equations of state (EOS): one that represents the best estimate for the sea water and two others for sensitivity tests. Most experiments focus on the first metres of the plume (6 m above the bottom) and one on the full extension (200 m span in the vertical). A particularity of the Basilisk code is to allow for varying spatial resolution, thanks to its octree data-structure (Figure 23c). We adjusted the resolution such that the minimal grid size is 1 cm in order to have the outlet spatially resolved. The code then adapts the resolution in time, adding more grid cells at places where the plume has small structures and coarsens it at quieter places and in the ambient stratification. To select the appropriate scale, we used a criterion based on the λ_2 value (Jeong, 1995). Figure 23a illustrates on a snapshot what λ_2 looks like and the non-uniform discretisation that results (Figure 23b). We used the Vreman (2004) model for the sub-grid scale closure. The turbulent Prandtl number is fixed at unity, implying that the diffusivity for heat and momentum are equal.

The time step dt of the simulation is limited by the smallest size cell for numerical stability, with dt~0.015 s. The time step limits the integration time on the hourly scale, which makes the simulation outside the range of the tide. The simulations with a zoom on the outlet and the one with the full extension are integrated over a period that is respectively ~9.5 and ~1.8 the vertical transit time, i.e. the time it takes for a particle to cross the domain in the vertical.

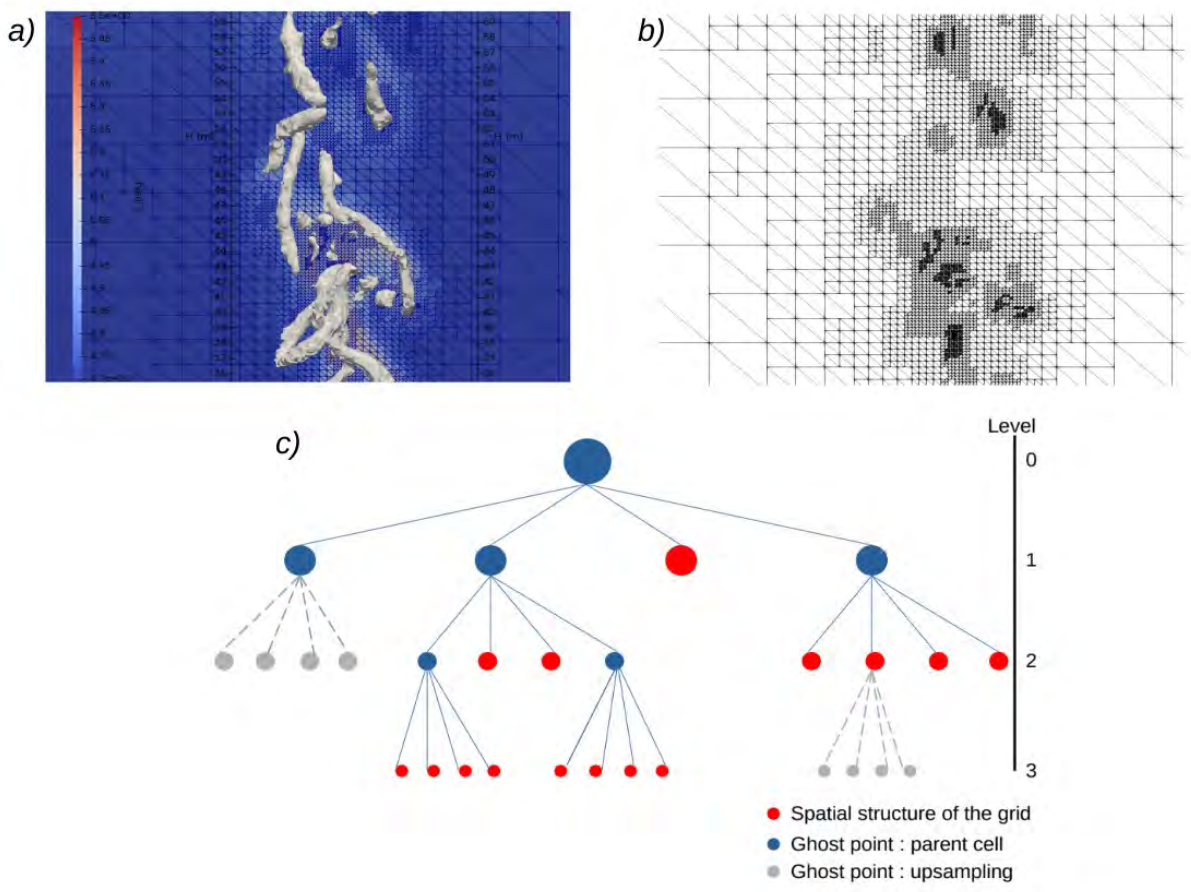

Figure 23. 3D coherent structure as revealed by the λ_2 parameter (a) that is used to define the level of grid refinement (b). The octree data structure is sketched in (c), where only a quadtree is shown for simplicity.

The results have been analysed offline. The vertical profiles are obtained by averaging horizontally over the plume area. Because of the turbulent nature of the plume, the plume boundary is not well defined. A criterion based on the temperature is not robust because the temperature difference between the plume and the environment becomes very small as the plume approaches its neutral level. Instead, we used a criterion based on w. The ambient stratification is quiescent when the plume can show both upward and downward speeds: the plume region is identified by its absolute velocity anomaly, such as $|w| >$ epsilon with epsilon set to 10^{-2} m s^{-1} after sensitivity experiments.

We diagnosed several key turbulent quantities, namely the entrainment rate and the energy dissipations rates. They are emerging properties of the simulations, directly controlling the mixing of water. The entrainment rate is characterised by the non-dimensional α coefficient. It is a measure, at a height z, of how much surrounding water is entrained into the plume relative to how much water is already rising within the plume. It is defined as $\alpha = w / u_e$, where w is averaged vertical velocity w and u_e the averaged horizontal inward flow at the plume boundary. It is a key factor for the MTT model. The two other key parameters are the kinetic energy dissipation rate ε_k and the potential energy dissipation rate ε_a. The former is computed by multiplying the velocity stress tensor with the velocity and the Vreman turbulent coefficient. The latter is computed following Winters et al. (1995), using the gradient of density, the ambient N^2 and the Vreman turbulent coefficient. The dissipation of potential energy is intimately linked to the mixing of density, viz. the diapycnal mixing rate. It is the energy that is 'taxed' from the flow and destroyed to mix two water parcels of different densities (Caulfield, 2021).

2.4. Results

Injection of turbulent kinetic energy (TKE)

The specification of constant flow rate at the outlet produces a plume that is highly unrealistic in the first metres (Figure 24c) because the plume is laminar in the first metre. This is because this boundary condition corresponds to the injection of a laminar flow. The turbulence kicks in downstream, at about 1 m above the outlet, after the shear instabilities have developed. In all images and videos of vents it is clear that the injected flow is turbulent from the outlet. This has to be modelled. We did this by adding a white noise in time on the injection velocity, namely $w=w_0(1+a\,W(t))$, where w_0 is the laminar input velocity, W(t) is a white noise signal, and a is the noise amplitude. Figure 24b shows the vertical profiles of TKE for various amplitudes. If the amplitude is too small, the turbulence does not start at the outlet. If the amplitude is too large, the result is an excess of TKE that gets quickly dissipated (Figure 24a). Even though we cannot rule out this possibility, it seems unlikely. The optimal value is a=50% for which the TKE varies smoothly, and the plume starts immediately turbulent (Figure 24d). The addition of a noise at the outlet is not a numerical fix, it is rather a parametrisation of the turbulence that is already present in the flow before it enters the ocean. This turbulence is not surprising as the spring is fed by a network of pipes in the ground, which are likely to be rough and not straight, encouraging turbulence. In addition, the Reynolds number at the outlet (Re=26,500) clearly indicates that the flow is already turbulent. For such inflow velocities (up to 1 m s^{-1}) the flow is turbulent. This injection of TKE corresponds to 12% of the injected KE.

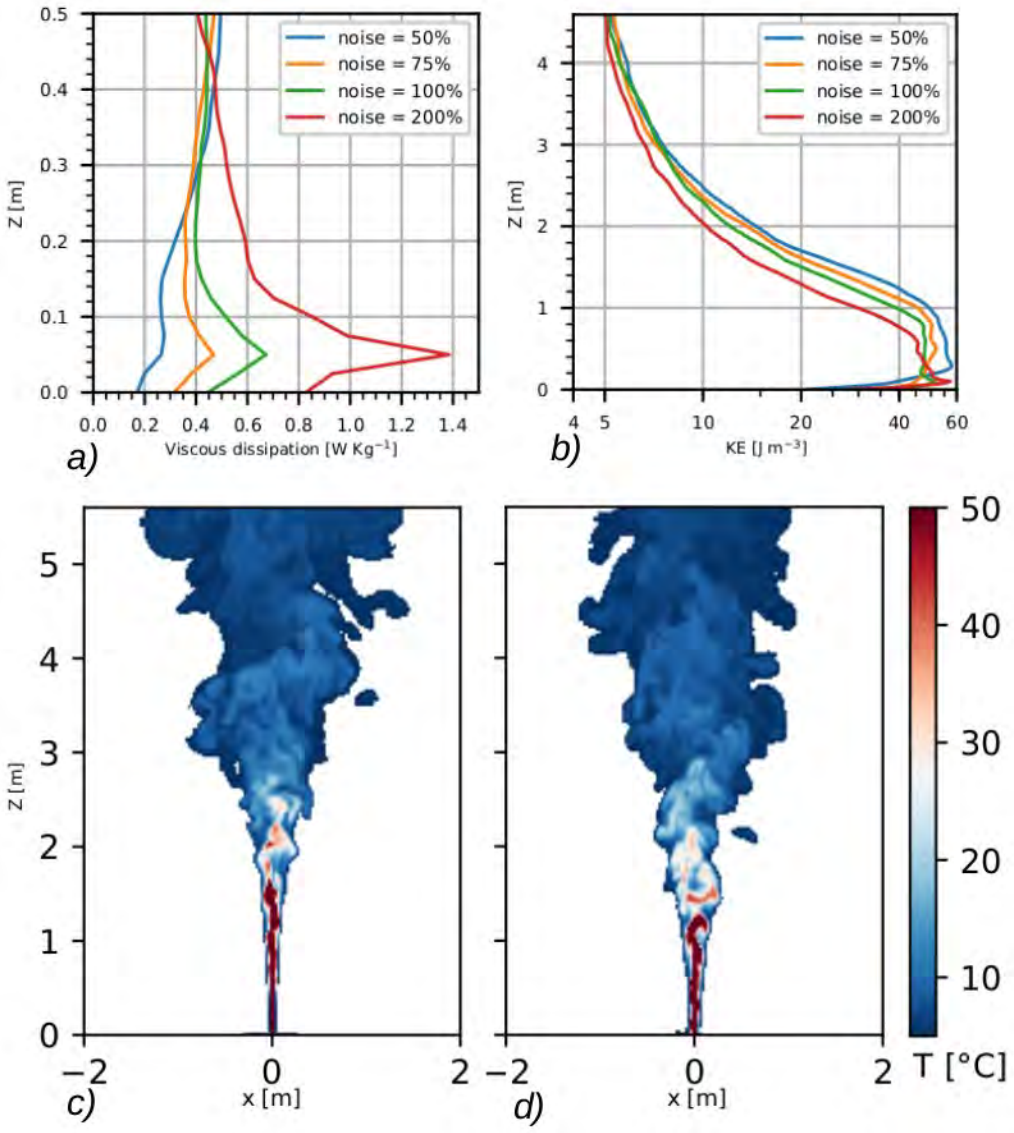

Figure 24. Vertical profiles of viscous dissipation (a), KE (b) and snapshots of temperature without injection of TKE (c) and with injection (d).

Effects of the seawater EOS nonlinearities

To have a correct plume dynamic, it is important that the density is properly related to the temperature. Indeed, the density is the quantity that enters in the momentum budget whereas the temperature is the quantity that is transported and mixed. The two are related via the equation of state (EOS). The sea water EOS is well tabulated in TEOS-10[1], but only in the so-called oceanic funnel, i.e. for reasonable temperature values. T=300°C is way out of this funnel. However, we found two papers that investigated the seawater EOS for larger values (Bischoff et al., 1985, Safarov et al., 2009). We combined them with TEOS-10 by using a smooth polynomial fit. The result is shown in Figure 25. The EOS is clearly not a linear relationship between density and temperature. To get insight on the importance of having the proper EOS, we tested two extreme EOS, both linear in temperature. The first is a linear extrapolation of TEOS-10, which overestimates the density at 300°C, and the second one is a linear interpolation from

[1] www.teos-10.org

T=300°C to TEOS-10 (Figure 25a), which reproduces the correct buoyancy flux at the exit, but misses all the nonlinearities.

Assessing the plume with a horizontal average is convenient for one-dimensional model comparison, and given the sharp drop in mean temperature at the exit from 300°C to 60°C, the simple linear extrapolation from TEOS-10 would be tempting, but a hot core of [200–250]°C is still present half a metre above the exit, reaching [100–150]°C at 1 m. Consequently, the non-linear effects of density changes still play an important role in the first metres. Our results show a braking effect (Figure 25b) for the simulation with the non-linear equation of state compared to the simulation with a linear equation and an equal buoyancy flux at the vent of about 25% on the velocity peak. The velocity profile is affected over the entire extent of the simulation at the exit scale (6 m). An appropriate equation of state is therefore necessary to correctly represent the volume flow in the water column.

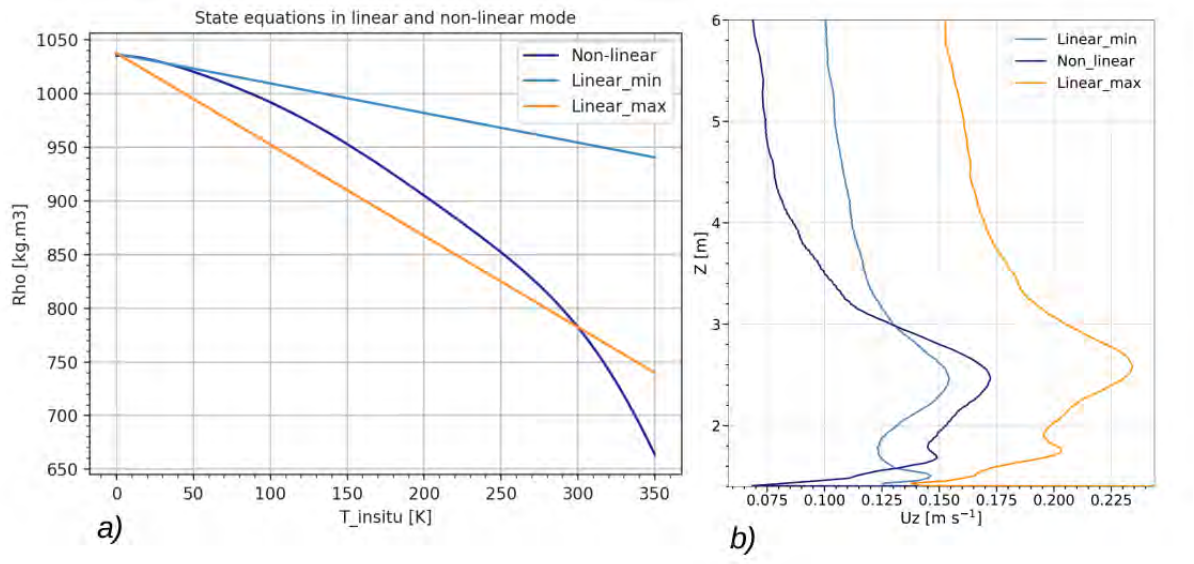

Figure 25. The three EOS used to compute the density (a) and the resulting velocity profiles (b). Nonlinear EOS (dark blue), linear extrapolation from TEOS-10 (blue) and linear interpolation from exact density at T-300°C (orange).

Height of the plume

The plume is usually characterised by the maximum altitude it can reach to attain the equilibration level. This is a key parameter that 1D models try to predict. But the speed gained during the ascension helps the plume to overshoot this altitude, before dissipating the excess of kinetic energy. The overshoot is typically observed by a negative temperature anomaly (Figure 26a). Under the hydrothermal conditions of LS, our results show that without cross-flow interaction, the plume of a single vent reaches its neutral buoyancy level (NBL) at 75 m. The powerful momentum overshoot allows the plume to reach an altitude above the seafloor H_{max} =135 m (Figure 26a). The large difference between the NBL and H_{max} is in fact an effect of the data average that smooths the extrema: the structure exhibits local positive temperature anomaly areas up to 120 m. The expected value of H_{max} based on the MTT model is 27 m: this gap can be explained by the conditions of the LS plume that are not fully compatible with the 1D model assumptions: non negligible momentum flux at the outlet, non-linear state equation, weak ambient stratification. Such limitation of the MTT model has already been reported in a similar context (Kaye, 2008).

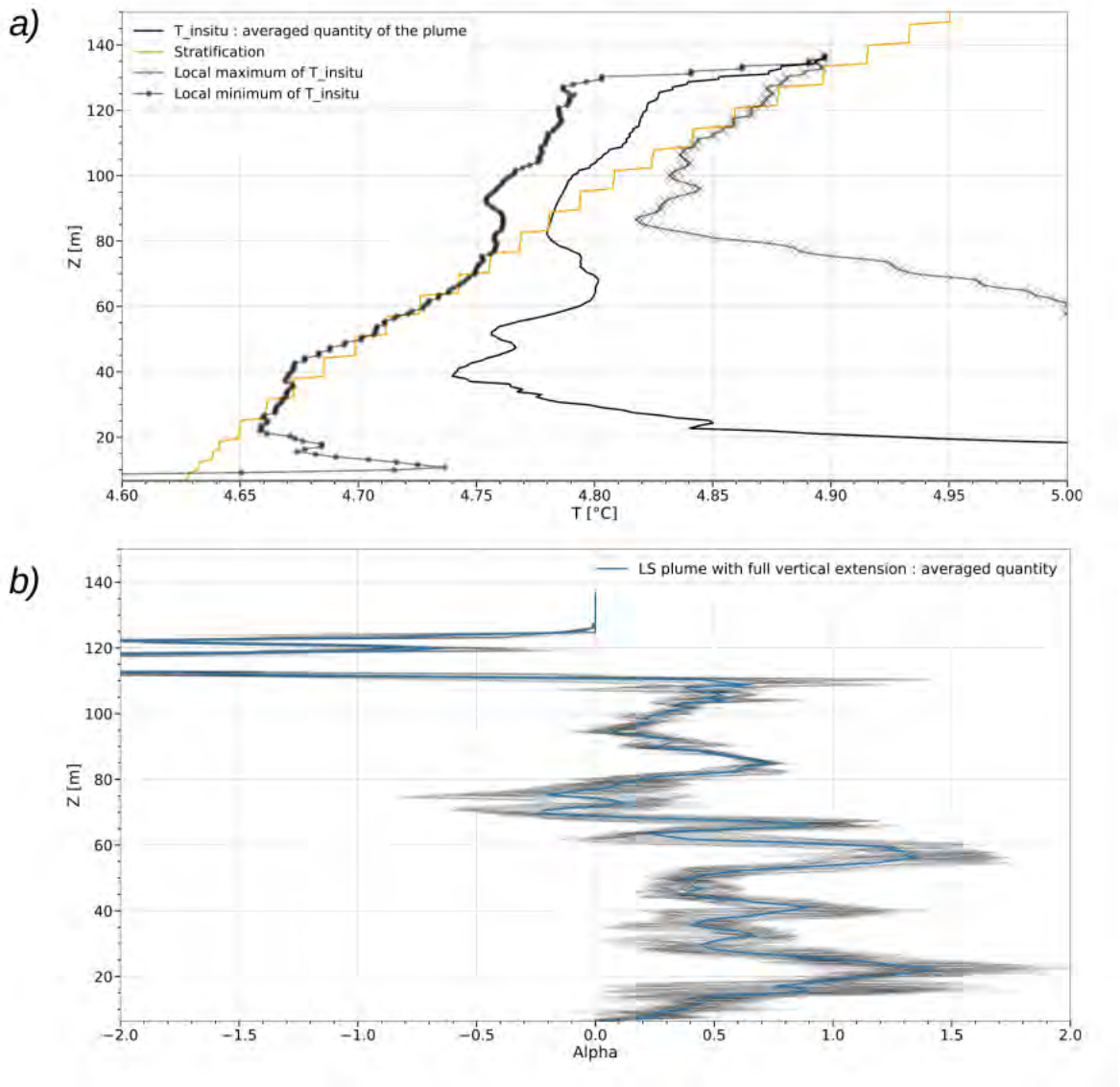

Figure 26. Vertical profiles of temperature (a) in the full vertical extension. Horizontal averaged in the plume (thin dark) and ambient (orange). In addition the extrema of temperature fluctuations are also represented: minimum (black circles) and maximum (grey crosses). Vertical profile of the entrainment coefficient α (b), superimposed with a low pass filter (blue) to smooth out the turbulent fluctuations.

Turbulent parameters

LES allows to diagnose all the quantities that are otherwise prescribed in more simplified models. A particular important parameter is the entrainment coefficient α. It is a direct measure of the dilution rate in LES, and for 1D model this value corresponds to a parametrisation of turbulence that drives the destruction of density variance during the ascent. There is no consensus on the exact value of α, and most work and experiments on plumes aim to determine this value. Plumes can be put into two categories: the 'lazy' plumes, that are driven by their excess of buoyancy anomaly, and the 'forced' plumes that are driven by their excess of momentum (Deremble, 2016). A parameter, Γ, can be calculated to evaluate the competition between the two forces as given by Morton and Middleton (1973): $\Gamma = r\ B\ /\ \alpha w^2$, with r being the radius of the exit and B representing buoyancy. At LS, this parameter ranges from 5 to 1,000, classifying the Lucky Strike vents as lazy plumes. In the LES presented here, this parameter is around Γ = 10, which is small enough for momentum effects to directly compete

with buoyancy at the exit, shaping the plume's behaviour. When the kinetic energy of the source is surpassed by buoyancy, the entrainment transitions from jet values to pure plume values. Our results show that α falls in the range of the classical value for a plume with a vertical dependence: α~0.04 in the momentum driven region, and reach α~0.13 in the buoyancy driven region (Figure 26b). The 0.13 value is very close to the one found by Devenish et al. (2010) using also LES on buoyant plumes.

The oceanic circulation at large scale depends on the mixing of warm and cold-water masses, which is driven by external forcing (wind and tide) through the breaking of internal waves. But this mixing is anisotropic and inhomogeneous (Smyth et al., 2001; Mashayek and Peltier, 2013), when its variations have a leading order of influence upon the rate of the abyssal meridional overturning circulation (Mashayek et al., 2017). For circulation models that are used to study climate change, this mixing occurs at the subgrid level and must be parametrised. The mixing is usually given in terms of mixing efficiency, based on the definition of Wykes et al. (2014), with the ratio $\eta=\varepsilon_A/(\varepsilon_A+\varepsilon_K)$ ith ε_A the dissipation rate of available potential energy (APE) and ε_K the dissipation rate of kinetic energy. In physical oceanography it is traditionally assumed that $\eta=0.17$, but more work is needed to fully capture this physical process (Caulfield, 2021).

The results show that the plume has a high potential energy at the source, correlated to a high value of mixing efficiency of $\eta=0.7$ at 10 m above the source. During the rise, ε_K takes control on the mixing over ε_A, reducing slowly the mixing efficiency. Our work confirms a boundary case where the prevalence of $\eta=0.17$ fails, confirming the plume as a potential source of high mixing efficiency that could contribute to enhance the overall mixing in the ocean.

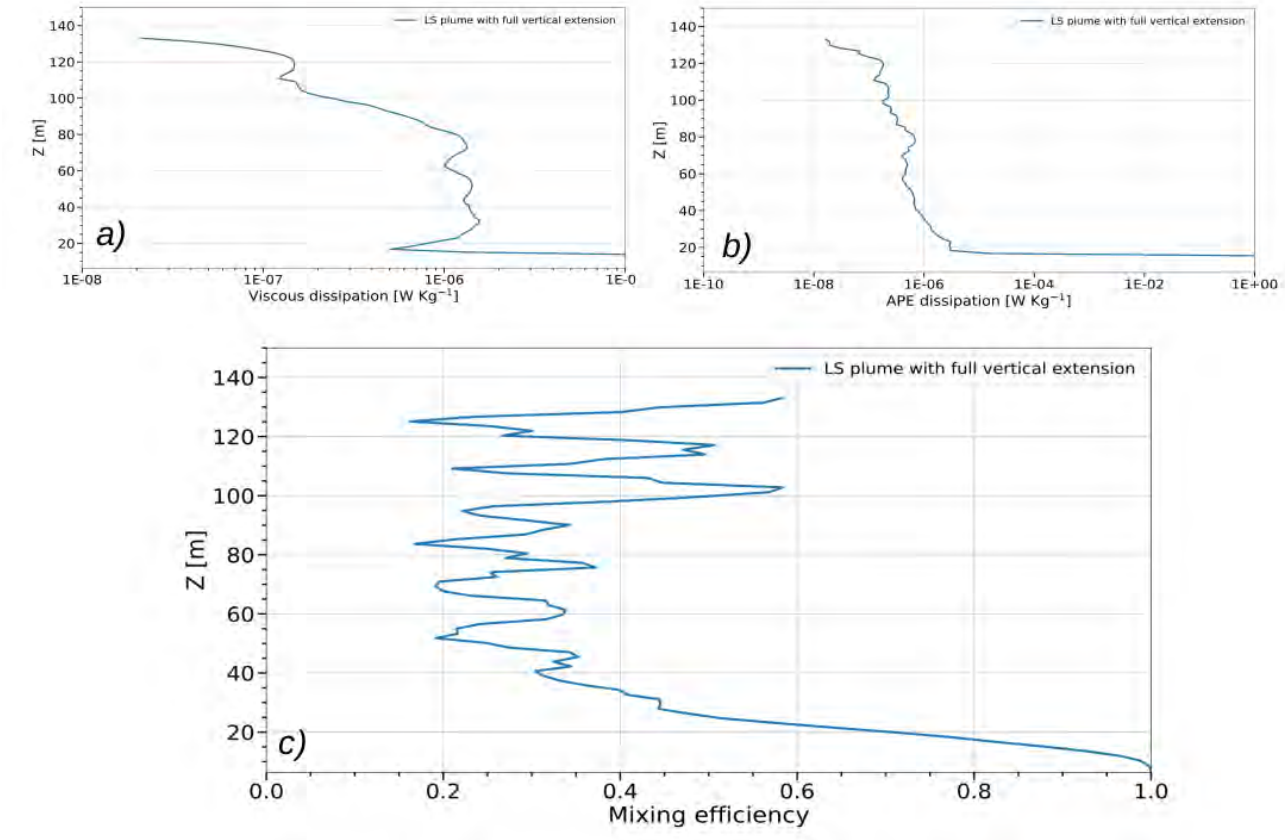

Figure 27. Vertical profiles of APE dissipation (a), KE dissipation (b) and mixing efficiency (c).

2.5. Discussion

The plume characteristics at LS are poorly known from in-situ measurements, mostly because it is very challenging to acquire high-resolution physical measurements within the plume. So far, the main source of information has been the video recordings (Van Audenhaege, 2018). The turbulence is clearly visible but only within the first 1 to 2 metres above the outlet. These videos provide a qualitative insight on the tip of the plume, but it is impossible to infer any quantitative variable from them. The LES is a tool to exploit these videos and extract quantitative information. The main information we wanted to extract was the flow rate, namely the vertical speed at the outlet times the outlet area. From the flow rate, it is then easy to deduce the associated heat flux. This objective, though potentially very useful, turned out to be more difficult than envisioned. This objective was not a deliverable of this work package, so we did not pursue it further. What our simulations have revealed, via the profile of entrainment coefficient, is that the first metres of the plume are dominated by the momentum input. In this narrow region, the plume is driven by the vertical velocity at the outlet, the outlet area and the injected TKE, which have been shown to account for 10–20% of the total TKE. We started exploring the parameter space (outlet velocity, outlet area) by doing one LES per point. From these LES we collate synthetic images such as Figure 22a that can then be compared directly to the video recordings. By matching the images, we can deduce the properties of the outlet, hence the associated heat flux.

Our simulations have shown that using an extension of TEOS-10 for very high temperature (up to 300K) only matters for the first five metres. Higher in the plume, the temperature fluctuations fall within the range of values that TEOS-10 cover. However, we have shown that in order to have the correct buoyancy flux, and hence the correct amount of potential energy input, it is important to have an EOS that gives a good estimate of the buoyancy at T=300°C, namely 780 kg m^{-3} at LS. Fitting this value to EOS with a basic linear interpolation does capture the main physics and compare quite well with a more appropriate polynomial fit. Our recommendation is to use a nonlinear EOS rather than an oversimplified linear EOS.

Our LES provide sound estimates of the entrainment coefficient, $\alpha \sim 0.13$ in the buoyancy driven region ($z>2$ m). This parameter is crucial in the 1D MTT model and would definitely be pivotal in any parametrisation of the plume. We found quite large mixing efficiency ($\eta=0.7$) in the lower part of the plume ($z \sim 10$ m) decreasing with height. This is consistent with previous findings (Gayen et al., 2013, Sohail et al., 2018) showing that convection enhances the mixing efficiency well above the standard assumed value of $\eta=0.17$ in the ocean. This result is explained by the fact that the energetics of the mixing is principally fed by the potential energy due to the buoyancy flux as the outlet, as opposed to kinetic energy driven for shear instabilities. As this matters for the mixing near the hydrothermal vents, this may also contribute to the global ocean mixing since hydrothermal vents are located mostly at medio-oceanic ridges, which are critical places for the diapycnal in the ocean (de Lavergne et al., 2016).

The neutral level of the plume (H=75 m) is larger than the one predicted by the MTT model (H=27 m), larger by a factor greater than two, but it is still less than the presumed observed 150 m height of the plume at LS. But because the plume overshoots, which is an expected behaviour, the water from the plume can be found up to 150 m above the source. In the absence of lateral currents, which is the case in our LES, the water within the overshoot falls back at the neutral level. However, it is uncertain whether this same water would also fall back if transported away by lateral currents, such as tidal currents or meso- and sub-mesoscale currents. Another surprising result is that a single vent has the ability to send water up to 150 m. This highlights the capacity for one single source to interact with the sub-mesoscale,

and potentially transport tracers at a long distance from the source. With the MTT predictions in mind, we could not imagine that one vent alone could yield such a rise. At LS, there are tens of vents, often gathered on edifices, such as Tour Eiffel, the one that motivated this study. The coalescence of the plumes at the scale of the edifice has also been started in this work package.

Finally, these results suggest new in-situ measurements to retrieve key parameters of the sources (velocity, temperature, diameter). Notably, one of the authors (Cyprien Lemaréchal) took part in the Momar23 field experiment. This is a yearly experiment to maintain the deep-sea observatory EMSO Azores, which operates on the seafloor using a ROV (Remotely Operated Vehicle). To test the LES simulations, some experiments have been carried out during this campaign. At the source scale (2,000 m depth), the gradients of temperature and the plume expansion were measured in the first 2 m with the ROV. The in-situ temperature gradients fall in the range of the data obtained in LES (Figure 28a), and with comparable outlet diameters, the expansion of the plume in LES follows the observations made close to the seafloor (Figure 28b).

Some measurements remain to be exploited to test our numerical results. A dye injection was performed to access the velocity field by a pseudo PIV. At a larger scale (200 m), CTD profiles were carried out close to the seafloor in order to measure vertical speed and temperature anomaly in real time, with the information of the 3D position of the measure.

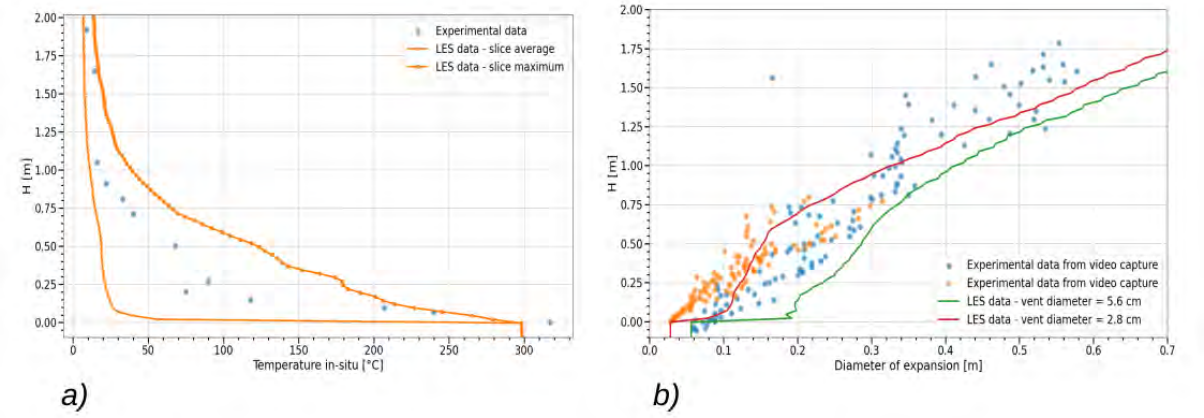

Figure 28. Vertical profiles of in-situ temperature (a) for LES (orange) and in-situ measurements (blue circles). The LES temperatures are the plume average (plain) and the maximum of fluctuations (dots). Vertical section of the plume diameter (b) for two LES outlets (green and red) and in-situ measurements (circles) for two vents.

Final summary and remarks

The regional-scale and local-scale models along the Walvis Ridge represent a well-established setup. The physical analyses concentrated on the description of near-bottom physical properties (e.g., temperature, salinity, currents) and proxies of physical processes (e.g., near-bottom kinetic energy dissipation and internal wave slope criticality), which are important predictors for benthic ecosystem communities and will help to improve the predictive skill of species distribution models in the future. In addition, the Lucky Strike vent field model represents an important step forward in the development of highest resolutions in the modelling of highly complex and dynamic benthic systems to come in the future. We engaged in LES of the vertical plume at the ultra-high resolution because this is very relevant for chemistry, biology and geophysics. From various discussions throughout the project, it became clear that such a study at very fine scales would be a valuable step forward and fill existing knowledge gaps. By focussing on the vertical plume, this study is a contribution to better comprehend how species, whether biological or chemical, are dispersed in the water column. A natural follow-up and application of this work is to design a protocol to retrieve the flow rate of a vent from a video. This retrieval will be made by matching the LES plume appearance with the image, such as Figure 22a. Both studies have shown specific merits, have provided new results, and highlight the importance of the spectrum of physical processes acting at fine and very fine spatial scales from hundreds of metres to less than tens of metres. The key results for each study area are summarised below.

Walvis Ridge seamounts:

- We developed nested high-resolution hydrodynamic models to simulate multi-year variations of bottom currents at two Walvis Ridge seamounts.
- We found that near-bottom currents are controlled by flow-topography interaction and internal tide dynamics.
- We suggest that physical processes such as kinetic energy dissipation and internal tide dynamics are suitable proxies of food supply to benthic filter feeding communities.

Lucky Strike:

- We have shown that the model should parametrise the turbulence within the ground in order to have a plume that is immediately turbulent, as seen in all video recordings of hydrothermal vents.
- We have shown that extending the EOS up to T=300°C, the temperature of the spring, was necessary to have the correct injection of potential energy.
- We have confirmed existing turbulent parameters, such as an entrainment rate of a=0.13 and large value of mixing efficiency (up to).
- We have shown that a single vent can send water up to 150 m in the overshoot, which is the height of the plume at LS. This is much larger than the basic MTT prediction, indicating that MTT model is a bit too simplistic for a quantitative prediction at LS.

References

Armstrong, C. W., Foley, N. S., Kahui, V., & Grehan, A. (2014). Cold water coral reef management from an ecosystem service perspective. *Marine Policy*, *50*, 126-134. https://doi.org/10.1016/j.marpol.2014.05.016

Artigue, L., Chavagnac, V., Destrigneville, C., Ferron, B., & Cathalot, C. (2022). Tracking the Lithium and Strontium Isotope Signature of Hydrothermal Plume in the Water Column: A Case Study at the EMSO-Azores Deep-Sea Observatory. *Frontiers in Environmental Chemistry*, *3*, 784385. https://doi.org/10.3389/fenvc.2022.784385

Barbet-Massin, M., Jiguet, F., Albert, C. H., & Thuiller, W. (2012). Selecting pseudo-absences for species distribution models: How, where and how many?. *Methods in ecology and evolution*, *3*(2), 327-338. https://doi.org/10.1111/j.2041-210X.2011.00172.x

Bergstad, O. A., Gil, M., Høines, Å. S., Sarralde-Vizuete, R., Maletzky, E., Mostarda, E., ... & Campanis, G. (2019a). Megabenthos and benthopelagic fishes on Southeast Atlantic seamounts, *African Journal of Marine Science*, 41(1), 29-50. https://doi.org/10.2989/1814232X.2019.1571439

Bergstad, O. A., Høines, Å. S., Sarralde, R., Campanis, G., Gil, M., Ramil, F., ... & António, M. A. (2019b). Bathymetry, substrate and fishing areas of Southeast Atlantic high-seas seamounts. *African Journal of Marine Science*, *41*(1), 11-28. https://doi.org/10.2989/1814232X.2019.1569160

Bischoff, J. L., & Rosenbauer, R. J. (1985). An empirical equation of state for hydrothermal seawater (3.2 percent NaCl). *American Journal of Science*, *285*(8), 725-763. https://doi.org/10.1146/annurev-fluid-042320-100458

Cacchione, D. A., Pratson, L. F., & Ogston, A. S. (2002). The shaping of continental slopes by internal tides. *Science*, *296*(5568), 724-727. https://doi.org/10.1126/science.1069803

Campanella, F., Collins, M. A., Young, E. F., Laptikhovsky, V., Whomersley, P., & van der Kooij, J. (2021). First insight of meso-and bentho-pelagic fish dynamics around remote seamounts in the South Atlantic Ocean. *Frontiers in Marine Science*, *8*, 663278. https://doi.org/10.3389/fmars.2021.663278

Caulfield, C. P. (2021). Layering, instabilities, and mixing in turbulent stratified flows. *Annual Review of Fluid Mechanics*, *53*, 113-145. https://doi.org/10.1146/annurev-fluid-042320-100458

Casanova-Masjoan, M., Pelegrí, J. L., Sangrà, P., Martínez, A., Grisolía-Santos, D., Pérez-Hernández, M. D., & Hernández-Guerra, A. (2017). Characteristics and evolution of an Agulhas ring, *Journal of Geophysical Research Oceans*, 122, 7049– 7065. https://doi.org/10.1002/2017JC012969

Chidichimo, M. P., Perez, R. C., Speich, S., Kersalé, M., Sprintall, J., Dong, S., ... & Schmid, C. (2023). Energetic overturning flows, dynamic interocean exchanges, and ocean warming observed in the South Atlantic. *Communications Earth & Environment*, *4*(1), 10. https://doi.org/10.1038/s43247-022-00644-x

Contreras, E., García, P. J., Sager, W. W., Thoram, S., Hoernle, K., Sarralde, R., & Zhou, H. (2022). Bathymetry of Valdivia Bank, Walvis Ridge, South Atlantic Ocean: Implications for structure and geologic history of a hot spot plateau. *Geochemistry, Geophysics, Geosystems*, *23*(11), Art-Nr. https://doi.org/10.1029/2022GC010624

Davies Wykes, M., Hughes, G., & Dalziel, S. (2015). On the meaning of mixing efficiency for buoyancy-driven mixing in stratified turbulent flows. *Journal of Fluid Mechanics, 781*, 261-275. https://doi.org/10.1017/jfm.2015.462

Davies, A. J., & Guinotte, J. M. (2011). Global habitat suitability for framework-forming cold-water corals. *PloS one*, *6*(4), e18483. https://doi.org/10.1371/journal.pone.0018483

de Froe, E., Maier, S. R., Horn, H. G., Wolff, G. A., Blackbird, S., Mohn, C., ... & van Oevelen, D. (2022). Hydrography and food distribution during a tidal cycle above a cold-water coral mound. *Deep Sea Research Part I: Oceanographic Research Papers*, *189*, 103854. https://doi.org/10.1016/j.dsr.2022.103854

de Lavergne, C., Madec, G., Le Sommer, J., Nurser, A. G., & Garabato, A. C. N. (2016). The impact of a variable mixing efficiency on the abyssal overturning. *Journal of Physical Oceanography*, *46*(2), 663-681. https://doi.org/10.1175/JPO-D-14-0259.1

Delandmeter, P., & Van Sebille, E. (2019). The Parcels v2. 0 Lagrangian framework: new field interpolation schemes. *Geoscientific Model Development*, *12*(8), 3571-3584. https://doi.org/10.5194/gmd-12-3571-2019

Dencausse, G., Arhan, M., & Speich, S. (2010). Routes of Agulhas rings in the southeastern Cape Basin. *Deep Sea Research Part I: Oceanographic Research Papers*, *57*(11), 1406-1421. https://doi.org/10.1016/j.dsr.2010.07.008

Deremble, B. (2016). Convective plumes in rotating systems. *Journal of Fluid Mechanics*, *799*, 27-55. https://doi.org/10.1017/jfm.2016.348

Devenish, B. J., Rooney, G. G., & Thomson, D. J. (2010). Large-eddy simulation of a buoyant plume in uniform and stably stratified environments. *Journal of Fluid Mechanics*, *652*, 75-103. https://doi.org/10.1017/S0022112010000017

Egbert, G. D., & Erofeeva, S. Y. (2002). Efficient inverse modeling of barotropic ocean tides. *Journal of Atmospheric and Oceanic technology*, *19*(2), 183-204. https://doi.org/10.1175/1520-0426(2002)019%3C0183:EIMOBO%3E2.0.CO;2

Flögel, S., Dullo, W. C., Pfannkuche, O., Kiriakoulakis, K., & Rüggeberg, A. (2014). Geochemical and physical constraints for the occurrence of living cold-water corals. *Deep Sea Research Part II: Topical Studies in Oceanography*, *99*, 19-26. https://doi.org/10.1016/j.dsr2.2013.06.006

Gayen, B., Griffiths, R. W., Hughes, G. O., & Saenz, J. A. (2013). Energetics of horizontal convection. *Journal of Fluid Mechanics*, *716*, R10. https://doi.org/10.1017/jfm.2012.592

Gevorgian, J., Sandwell, D. T., Yu, Y., Kim, S. S., & Wessel, P. (2023). Global distribution and morphology of small seamounts. *Earth and Space Science*, *10*(4), e2022EA002331. https://doi.org/10.1029/2022EA002331

Jeong, J., & Hussain, F. (1995). On the identification of a vortex. *Journal of fluid mechanics*, *285*, 69-94. https://doi.org/10.1017/S0022112095000462

Kaye, N. B. (2008). Turbulent plumes in stratified environments: a review of recent work. *Atmosphere--Ocean (Canadian Meteorological & Oceanographic Society)*, *46*(4). https://doi.org/10.3137/AO923.2008

Khripounoff, A., Caprais, J. C., Le Bruchec, J., Rodier, P., Noel, P., & Cathalot, C. (2014). Deep cold-water coral ecosystems in the Brittany submarine canyons (Northeast Atlantic): Hydrodynamics, particle supply, respiration, and carbon cycling. *Limnology and oceanography*, *59*(1), 87-98. https://doi.org/10.4319/lo.2014.59.1.0087

Knudby, A., Kenchington, E., & Murillo, F. J. (2013). Modeling the distribution of Geodia sponges and sponge grounds in the Northwest Atlantic. *PloS one*, *8*(12), e82306. https://doi.org/10.1371/journal.pone.0082306

Liu, M., & Tanhua, T. (2021). Water masses in the Atlantic Ocean: characteristics and distributions. *Ocean Science*, *17*(2), 463-486. https://doi.org/10.5194/os-17-463-2021

López-Abellán, L. J., Holtzhausen, J. A., Agudo-Bravo, L. M., Jiménez, P., Sanz-Alonso, J. L., González-Porto, M., ... & Ferrer, M. (2011). Preliminary report of the multidisciplinary research cruise on the Walvis Ridge seamounts (Atlantic Southeast-SEAFO).

Mashayek, A., & Peltier, W. R. (2013). Shear-induced mixing in geophysical flows: does the route to turbulence matter to its efficiency?. *Journal of Fluid Mechanics*, *725*, 216-261. https://doi.org/10.1017/jfm.2013.176

Mashayek, A., Salehipour, H., Bouffard, D., Caulfield, C. P., Ferrari, R., Nikurashin, M., ... & Smyth, W. D. (2017). Efficiency of turbulent mixing in the abyssal ocean circulation. *Geophysical Research Letters*, *44*(12), 6296-6306. https://doi.org/10.1002/2016GL072452

McQuaid, K. A., Bridges, A. E., Howell, K. L., Gandra, T. B., de Souza, V., Currie, J. C., ... & Yool, A. (2023). Broad-scale benthic habitat classification of the South Atlantic. *Progress in oceanography*, *214*, 103016. https://doi.org/10.1016/j.pocean.2023.103016

Mienis, F., De Stigter, H. C., White, M., Duineveld, G., De Haas, H., & Van Weering, T. C. E. (2007). Hydrodynamic controls on cold-water coral growth and carbonate-mound development at the SW and SE Rockall Trough Margin, NE Atlantic Ocean. *Deep Sea Research Part I: Oceanographic Research Papers*, *54*(9), 1655-1674. https://doi.org/10.1016/j.dsr.2007.05.013

Mohn, C., Hansen, J. L., Carreiro-Silva, M., Cunningham, S. A., de Froe, E., Dominguez-Carrió, C., ... & van Oevelen, D. (2023). Tidal to decadal scale hydrodynamics at two contrasting cold-water coral sites in the Northeast Atlantic. *Progress in Oceanography*, *214*, 103031. https://doi.org/10.1016/j.pocean.2023.103031

Morato, T., González-Irusta, J. M., Dominguez-Carrió, C., Wei, C. L., Davies, A., Sweetman, A. K., ... & Carreiro-Silva, M. (2020). Climate-induced changes in the suitable habitat of cold-water corals and commercially important deep-sea fishes in the North Atlantic. *Global Change Biology*, *26*(4), 2181-2202. https://doi.org/10.1111/gcb.14996

Morton, B. R., & Middleton, J. (1973). Scale diagrams for forced plumes. *Journal of Fluid Mechanics*, *58*(1), 165-176. https://doi.org/10.1017/S002211207300220X

Morton, B. R., Taylor, G. I., & Turner, J. S. (1956). Turbulent gravitational convection from maintained and instantaneous sources. *Proceedings of the Royal Society of London. Series A. Mathematical and Physical Sciences*, *234*(1196), 1-23. https://doi.org/10.1098/rspa.1956.0011

Muñoz, P. D., Sayago-Gil, M., Murillo, F. J., Del Río, J. L., López-Abellán, L. J., Sacau, M., & Sarralde, R. (2012). Actions taken by fishing Nations towards identification and protection of vulnerable marine ecosystems in the

high seas: The Spanish case (Atlantic Ocean). *Marine Policy*, *36*(2), 536-543. https://doi.org/10.1016/j.marpol.2011.09.005

Popinet, S. (2018). Basilisk 18-02-16. https://doi.org/10.5281/zenodo.1203631

Roberts, J. M., & Cairns, S. D. (2014). Cold-water corals in a changing ocean. *Current Opinion in Environmental Sustainability*, *7*, 118-126. https://doi.org/10.1016/j.cosust.2014.01.004

Rogers, A. D. (2018). The biology of seamounts: 25 years on. *Advances in marine biology*, *79*, 137-224. https://doi.org/10.1016/bs.amb.2018.06.001

Rühs, S., Schwarzkopf, F. U., Speich, S., & Biastoch, A. (2019). Cold vs. warm water route–sources for the upper limb of the Atlantic Meridional Overturning Circulation revisited in a high-resolution ocean model. *Ocean Science*, *15*(3), 489-512. https://doi.org/10.5194/os-15-489-2019

Rühs, S., Schmidt, C., Schubert, R., Schulzki, T. G., Schwarzkopf, F. U., Le Bars, D., & Biastoch, A. (2022). Robust estimates for the decadal evolution of Agulhas leakage from the 1960s to the 2010s. *Communications Earth & Environment*, *3*(1), 318. https://doi.org/10.1038/s43247-022-00643-y

Safarov, J., Millero, F., Feistel, R., Heintz, A., & Hassel, E. (2009). Thermodynamic properties of standard seawater: extensions to high temperatures and pressures. *Ocean Science*, *5*(3), 235-246. https://doi.org/10.5194/os-5-235-2009

Schulz, K., Soetaert, K., Mohn, C., Korte, L., Mienis, F., Duineveld, G., & van Oevelen, D. (2020). Linking large-scale circulation patterns to the distribution of cold water corals along the eastern Rockall Bank (northeast Atlantic). *Journal of Marine Systems*, *212*, 103456. https://doi.org/10.1016/j.jmarsys.2020.103456

Schumacher, M., Huvenne, V. A., Devey, C. W., Arbizu, P. M., Biastoch, A., & Meinecke, S. (2022). The Atlantic Ocean landscape: A basin-wide cluster analysis of the Atlantic near seafloor environment. *Frontiers in Marine Science*, *9*, 936095. https://doi.org/10.3389/fmars.2022.936095

Schwarzkopf, F. U., Biastoch, A., Böning, C. W., Chanut, J., Durgadoo, J. V., Getzlaff, K., ... & Schubert, R. (2019). The INALT family–a set of high-resolution nests for the Agulhas Current system within global NEMO ocean/sea-ice configurations. *Geoscientific Model Development*, *12*(7), 3329-3355. https://doi.org/10.5194/gmd-12-3329-2019

SEAFO (2019). Dr Fridtjof Nansen Survey 2019 – Cruise Report. SEAFO 15th Scientific Committee Meeting. DOC/SC/05/2019. Swakopmund, Namibia.

SEAFO (2022). Dr Fridtjof Nansen Survey 2022 – Cruise Report. SEAFO 18th Scientific Committee Meeting. DOC/SC/03/2022. Swakopmund, Namibia.

Shchepetkin, A. F., & McWilliams, J. C. (2005). The regional oceanic modeling system (ROMS): a split-explicit, free-surface, topography-following-coordinate oceanic model. *Ocean modelling*, *9*(4), 347-404. https://doi.org/10.1016/j.ocemod.2004.08.002

Smyth, W. D., Moum, J. N., & Caldwell, D. R. (2001). The efficiency of mixing in turbulent patches: Inferences from direct simulations and microstructure observations. *Journal of Physical Oceanography*, *31*(8), 1969-1992. https://doi.org/10.1175/1520-0485(2001)031%3C1969:TEOMIT%3E2.0.CO;2

Soetaert, K., Mohn, C., Rengstorf, A., Grehan, A., & van Oevelen, D. (2016). Ecosystem engineering creates a direct nutritional link between 600-m deep cold-water coral mounds and surface productivity. *Scientific reports*, *6*(1), 35057. https://doi.org/10.1038/srep35057

Sohail, T., Gayen, B., & Hogg, A. M. (2018). Convection enhances mixing in the Southern Ocean. *Geophysical Research Letters*, *45*(9), 4198-4207. https://doi.org/10.1029/2018GL077711

St. Laurent, L. S., & Garrett, C. (2002). The role of internal tides in mixing the deep ocean. *Journal of physical oceanography*, *32*(10), 2882-2899. https://doi.org/10.1175/1520-0485(2002)032%3C2882:TROITI%3E2.0.CO;2

Stramma, L., & England, M. (1999). On the water masses and mean circulation of the South Atlantic Ocean. *Journal of Geophysical Research: Oceans*, *104*(C9), 20863-20883. https://doi.org/10.1029/1999JC900139

Sundahl, H., Buhl-Mortensen, P., & Buhl-Mortensen, L. (2020). Distribution and suitable habitat of the cold-water corals *Lophelia pertusa*, *Paragorgia arborea*, and *Primnoa resedaeformis* on the Norwegian continental shelf. *Frontiers in Marine Science*, 213. https://doi.org/10.3389/fmars.2020.00213

Tim, N., Zorita, E., Schwarzkopf, F. U., Rühs, S., Emeis, K. C., & Biastoch, A. (2018). The impact of Agulhas leakage on the central water masses in the Benguela upwelling system from a high-resolution ocean simulation. *Journal of Geophysical Research: Oceans*, *123*(12), 9416-9428. https://doi.org/10.1029/2018JC014218

Tsujino, H., Urakawa, S., Nakano, H., Small, R. J., Kim, W. M., Yeager, S. G., ... & Yamazaki, D. (2018). JRA-55 based surface dataset for driving ocean–sea-ice models (JRA55-do). *Ocean Modelling*, *130*, 79-139. https://doi.org/10.1016/j.ocemod.2018.07.002

Van Audenhaege L., Arnaubec A., & Matabos M. (2018). Eiffel Tower hydrothermal edifice of 2018 (Lucky Strike hydrothermal vent field, Mid Atlantic Ridge): 3D scene and imagery. SEANOE. https://doi.org/10.17882/92215

van Heuven, S. M., Hoppema, M., Huhn, O., Slagter, H. A., & de Baar, H. J. (2011). Direct observation of increasing CO2 in the Weddell Gyre along the Prime Meridian during 1973–2008. *Deep Sea Research Part II: Topical Studies in Oceanography*, *58*(25-26), 2613-2635. https://doi.org/10.1016/j.dsr2.2011.08.007

Vreman, A. W. (2004). An eddy-viscosity subgrid-scale model for turbulent shear flow: Algebraic theory and applications. *Physics of fluids*, *16*(10), 3670-3681. https://doi.org/10.1063/1.1785131

Wessel, P., Sandwell, D. T., Kim, S. S. (2010). The global seamount census. Oceanography, 23(1), 24-33. https://doi.org/10.5670/oceanog.2010.60

Document Information

EU Project N°	818123	**Acronym**	iAtlantic
Full Title	Integrated Assessment of Atlantic Marine Ecosystems in Space and Time		
Project website	www.iatlantic.euhttp:		

Deliverable	**N°**	1.3	**Title**	Quantitative assessment of near-seafloor flow dynamics and physical drivers for material and larval transport
Work Package	**N°**	1	**Title**	Atlantic Oceanography and Ecosystem Connectivity

Date of delivery	**Contractual**	Month 57	**Actual**	Month 57
Dissemination level	**PU**	**PU Public, fully open, e.g. web**		
		CO Confidential restricted under conditions set out in Model Grant Agreement		
		CI Classified, information as referred to in Commission Decision 2001/844/EC		

Authors (Partner(s))	Christian Mohn, Franziska Schwarzkopf, Patricia Garcia Jimenez, Cova Orejas, Veerle Huvenne, Mia Schumacher, Irene Pérez-Rodríguez, Roberto Sarralde Vizuete, Luis J. López Abellán, Pedro Vélez Belchí, Andy Dale, Colin Devey, Lisa Skein, Jørgen L.S. Hansen, Eva Friis Møller, Arne Biastoch, Cyrien Lemaréchal, Guillaume Roullet, Jonathan Gula			
Responsible Authors	**Names**	Guillaume Roullet Christian Mohn	**Emails**	guillaume.roullet@univ-brest.fr chmo@ecos.au.dk